

# Negative autoregulation matches production and demand in synthetic transcriptional networks

Experimental methods, data processing, and modeling

Elisa Franco<sup>1,\*</sup>, Giulia Giordano<sup>2</sup>, Per-Ola Forsberg<sup>3</sup>, and Richard M. Murray<sup>4</sup>

<sup>1</sup>*Mechanical Engineering, University of California at Riverside, Riverside, CA 92521*

<sup>2</sup>*Department of Mathematics and Computer Science, University of Udine, Italy*

<sup>3</sup>*Kristianstad Central Hospital, 29832 Tollarp, Sweden*

<sup>4</sup>*Engineering and Applied Science, California Institute of Technology, Pasadena, CA 91125*

*\*Corresponding author*

October 4, 2013

# Contents

<b>1</b>	<b>Experimental implementation of a two-gene flux matching system based on negative autoregulation: Materials and methods</b>	<b>3</b>
1.1	Reactions and domains design . . . . .	3
1.2	Oligonucleotide sequences . . . . .	3
1.3	DNA oligonucleotides and enzymes . . . . .	5
1.4	Transcription protocol . . . . .	5
1.5	Data acquisition and processing . . . . .	5
1.6	Characterization assays . . . . .	6
1.6.1	Genelets in isolation . . . . .	6
1.6.2	Interconnected genelets . . . . .	6
1.6.3	Flux adaptation . . . . .	8
1.6.4	Data fitting . . . . .	8
<b>2</b>	<b>Modeling and numerical analysis: two-gene flux matching system</b>	<b>11</b>
2.1	Simple model system: derivation of nullclines and rate matching conditions . . .	11
2.2	Differential equations modeling the experimental implementation . . . . .	13
<b>3</b>	<b>Modeling and numerical analysis: Scalability of the negative feedback scheme for flux regulation</b>	<b>20</b>
3.1	Simple model system . . . . .	20
3.1.1	Single product topology . . . . .	20
3.1.2	Handshake and neighbor topologies . . . . .	22
3.1.3	Parameters . . . . .	22
3.1.4	Performance overview of the different topologies as a function of key parameters . . . . .	22
<b>4</b>	<b>Positive feedback architecture for a two-gene system. Modeling and a viable experimental implementation</b>	<b>26</b>
4.1	Simple model system: derivation of nullclines and rate matching conditions . . .	26
4.2	A possible experimental implementation of a two-gene positive feedback scheme	28
4.2.1	Modeling . . . . .	30
<b>5</b>	<b>Numerical scalability analysis of our simplified positive feedback scheme model for flux regulation</b>	<b>33</b>
5.1	Single product topology . . . . .	34
5.2	Handshake and neighbor topologies . . . . .	35
5.3	Parameters . . . . .	35
5.4	Performance overview of the different topologies as a function of key parameters	35

# 1 Experimental implementation of a two-gene flux matching system based on negative autoregulation: Materials and methods

## 1.1 Reactions and domains design

A graphical sketch of the domain-level design for the self-repression interconnection is shown in Figure S1 A. The RNA outputs of each genelet are designed so that:

- 1) Each RNA output has a domain complementary to its activator strand.
- 2) The two RNA species are also complementary.

These specifications introduce a binding domain between  $T_i$  and  $R_j$ , which is considered another off state, as shown in Figure S1 B. Such a complex is a substrate for RNase H and the RNA strand is degraded by the enzyme, releasing the genelet activation domain. We assume that the transcription efficiency of an RNA-DNA promoter complex is very low. This hypothesis was not experimentally challenged for this specific system; however data shown in Franco et al. [2011], Supplementary Information, show that this assumption is valid for other genelets with the same promoter domain.

The design of a self-inhibiting genelet was first characterized in Kim [2007]. The circuit design proposed here, with two-domain RNA transcripts, was originally presented in Franco et al. [2008].

DNA strands were designed by thermodynamic analysis using the Winfree lab DNA design toolbox for MATLAB, Nupack Zadeh et al. [2011] and Mfold Zuker and Stiegler [1981]. The strands were optimized to yield free energy gains favoring the desired reactions, and to avoid unwanted secondary structures and crosstalk. Further constraints on the length and structure of the strands, which can affect the transcription efficiency and fidelity, were taken into account referring to Kim [2007], Chapter 3.4.

## 1.2 Oligonucleotide sequences

Due to technical constraints of the supplier IDT DNA,  $T_1 - nt$  and  $T_2 - nt$  were shortened with respect to the nominal design to have a length of 125 bases. The strands used in the experiments are those denoted below as "Short". These modifications did not alter the regulatory domains of the transcripts  $R_1$  and  $R_2$ . Also the full length of the main transcription products was not affected, as verified by gel electrophoresis in Figure S2 B.

**$T_1$ -nt** Full (134-mer) 5'-CTA ATG AAC TAC TAC TAC ACA CTA ATA CGA CTC ACT ATA GGG AGA AAC AAG AAC GAC ACT AAT GAA CTA CTA CTA CAC ACC AAC CAC AAC TTT ACC TTA ACC TTA CTT ACC ACG GCA GCT GAC AAA GTC AGA AA-3' (not synthesized)

**$T_1$ -nt** Short (125-mer) 5'-Tamra-CT AAT GAA CTA CTA CTA CAC ACT AAT ACG ACT CAC TAT AGG GAG AAA CAA GAA CGA CAC TAA TGA ACT ACT ACT ACA CAC CAA CCA CAA CTT TAC CTT AAC CTT ACT TAC CAC GGC AGC TGA CAA-3'

**$T_1$ -t** (107-mer) 5'-TTT CTG ACT TTG TCA GCT GCC GTG GTA AGT AAG GTT AAG GTA AAG TTG TGG TTG GTG TGT AGT AGT AGT TCA TTA GTG TCG TTC TTG TTT CTC CCT ATA GTG AGT CG-3'

**$A_1$**  (35-mer) 5'-TAT TAG TGT GTA GTA GTA GTT CAT TAG TGT CGT TC-3'

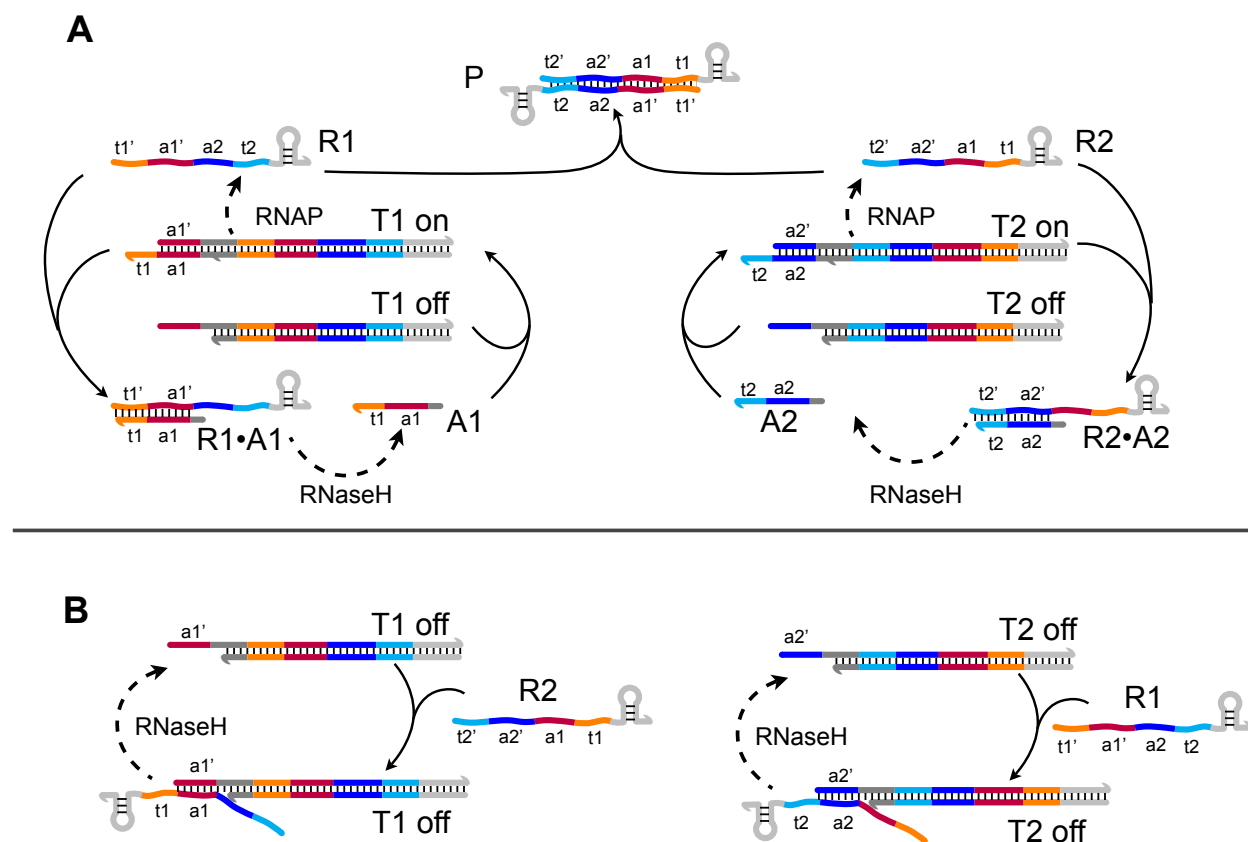


Figure S1: General reaction scheme representing a transcriptional circuit implementation of the two-gene negative feedback scheme for flux matching. Complementary domains have the same color. Promoters are in dark gray, terminator hairpin sequences in light gray. The RNA output of each genelet is designed to be complementary to its corresponding activator strand. The two RNA species are also complementary. A. Desired self-inhibition loops. B. Undesired cross-hybridization and RNase H mediated degradation of the RNA-template complexes.

**T<sub>2</sub>-nt** Full (126-mer) 5'-GGT TAA GGT AAA GTT GTG GTT GTA ATA CGA CTC ACT ATA GGG AGA AAC AAG TAA GTA AGG TTA AGG TAA AGT TGT GGT TGG TGT GTA GTA GTA GTT CAT TAG TGT CGT TCC TGA CAA AGT CAG AAA-3' (not synthesized)

**T<sub>2</sub>-nt** Short (126-mer) 5'-TexasRed-GG TTA AGG TAA AGT TGT GGT TGT AAT ACG ACT CAC TAT AGG GAG AAA CAA GTA AGT AAG GTT AAG GTA AAG TTG TGG TTG GTG TGT AGT AGT AGT TCA TTA GTG TCG TTC CTG ACA AAG TCA GAA-3'

**T<sub>2</sub>-t** (99-mer) 5'-TTT CTG ACT TTG TCA GGA ACG ACA CTA ATG AAC TAC TAC TAC ACA CCA ACC ACA ACT TTA CCT TAA CCT TAC TTA CTT GTT TCT CCC TAT AGT GAG TCG-3'

**A<sub>2</sub>** (35-mer) 5'-TAT TAC AAC CAC AAC TTT ACC TTA ACC TTA CTT AC-3'

**R<sub>1</sub>** (95-mer) 5' - GGG AGA AAC AAG AAC GAC ACU AAU GAA CUA CUA CUA CAC ACC AAC CAC AAC UUU ACC UUA ACC UUA CUU ACC ACG GCA GCU GAC AAA GUC AGA AA -3'

**R<sub>2</sub>** (87-mer) 5'-GGG AGA AAC AAG UAA GUA AGG UUA AGG UAA AGU UGU GGU UGG UGU GUA GUA GUA GUU CAU UAG UGU CGU UCC UGA CAA AGU CAG AAA -3'

### 1.3 DNA oligonucleotides and enzymes

All the strands were purchased from Integrated DNA Technologies, Coralville, IA IDT.  $T_1 - nt$  is labeled with TAMRA at the 5' end,  $T_2 - nt$  is labeled with Texas Red at the 5' end, both activators  $A_1$  and  $A_2$  are labeled with the IOWA black RQ quencher at the 3' end. The transcription buffer mix was prepared prior to each experiment run (two to four samples) using the T7 Megashortscript kit (#1354), Ambion, Austin, TX which includes the T7 RNA polymerase enzyme mix, the transcription buffer, and rNTPs utilized in the experiments. *E. coli* RNase H was purchased from Ambion (#2292).

### 1.4 Transcription protocol

The templates were annealed with 10% (v/v) 10× transcription buffer from 90°C to 37°C for 1 h 30 min at a concentration 5–10× the target concentration. The DNA activators were added to the annealed templates from a higher concentration stock, in a solution with 10% (v/v), 10× transcription buffer, 7.5 mM each NTP, 4% (v/v) T7 RNA polymerase, and .44% (v/v) *E. coli* RNase H. Each transcription experiment for fluorescence spectroscopy was prepared for a total target volume of 70  $\mu$ l. Samples for gel studies were quenched using a denaturing dye (80% formamide, 10 mM EDTA, 0.01g XCFF).

### 1.5 Data acquisition and processing

The fluorescence was measured at 37°C every two minutes with a Horiba/Jobin Yvon Fluorolog 3 system. Excitation and emission maxima for TAMRA were set to 559 nm and 583 nm, respectively, according to the IDT recommendation; for Texas Red the maxima for the spectrum were set to 598–617 nm. Slit widths were set to 2 nM for excitation and 4 nM for emission. The raw fluorescence data  $\Phi(t)$  were converted to estimated switch activity by normalizing with respect to maximum fluorescence  $\Phi_{\max}$  (measured before adding activators and enzymes) and to minimum

fluorescence  $\Phi_{\min}$  (measured after adding activators and before adding enzymes):

$$[T_i A_i](t) = [T_i^{tot}] \cdot \left( 1 - \frac{\Phi(t) - \Phi_{\min}}{\Phi_{\max} - \Phi_{\min}} \right).$$

For the adaptation experiments, normalization was done by measuring maximum and minimum fluorescence levels at the beginning of the experiment, and assuming that the maximum fluorescence level scales linearly with the change in total fluorescently labeled strands, while the minimum is not significantly affected by that variation. We used the formula:

$$[T_i A_i](t) = \alpha [T_i^{tot}] \cdot \left( 1 - \frac{\Phi(t) - \Phi_{\min}}{\alpha \Phi_{\max} - \Phi_{\min}} \right),$$

where  $\alpha$  is a factor that scales the total amount of template as it varies in the experiment.

Denaturing polyacrylamide gels (8% 19:1 acrylamide:bis and 7 M urea in TBE buffer, 100 mM Tris, 90 mM boric acid, 1 mM EDTA) were run at 67°C for 45 min with 10 V/cm in TBE buffer. Samples were loaded using Xylene Cyanol FF dye. For quantitation, denaturing gels were stained with SYBR Gold (Molecular Probes, Eugene, OR; #S-11494). In the control lane a 10-base DNA ladder (Invitrogen, Carlsbad, CA; #1082-015) was utilized. The DNA ladder 100 bp band was used as a control to roughly estimate the concentrations of the RNA species in solution in Figure S4 E and F. Gels were scanned using the Molecular Imager FX (Biorad, Hercules, CA) and analyzed using the Quantity One software (Biorad, Hercules, CA).

## 1.6 Characterization assays

This section reports experimental results and numerical fits. All experiments were run in triplicates: mean and error bars (standard deviation) are shown in each figure, together with the simulated traces (dashed lines) from our fitted model. The full derivation for the model fitted to the data is in Section 2.2.

### 1.6.1 Genelets in isolation

Figure S2 A shows the behavior of the two genelets in isolation: we can verify that each genelet self-inhibits after the enzymes are added. (For details on the data normalization procedure, refer to Section 1.5.) The concentration of RNA present in solution can be measured through gel electrophoresis, as shown in Figure S2 B: lanes 1 and 2 show that free RNA in solution is effectively absent.

### 1.6.2 Interconnected genelets

When the two genelets are present in solution in stoichiometric amount, their RNA outputs bind quickly to form a double-stranded complex, and therefore the feedback loops become a secondary reaction (by design thermodynamically less favorable than the  $R_1 \cdot R_2$  complex formation). As shown in Figure S2 C, the two genelets only moderately self-repress. The total RNA concentration in solution is high, as shown in the denaturing gel in Figure S2 B, lanes 3 and 4.

When the templates  $[T_1^{tot}]$  and  $[T_2^{tot}]$  are in different ratios, the system behavior is shown in Figure S3. We can plot the resulting initial active template ratio (which corresponds to the

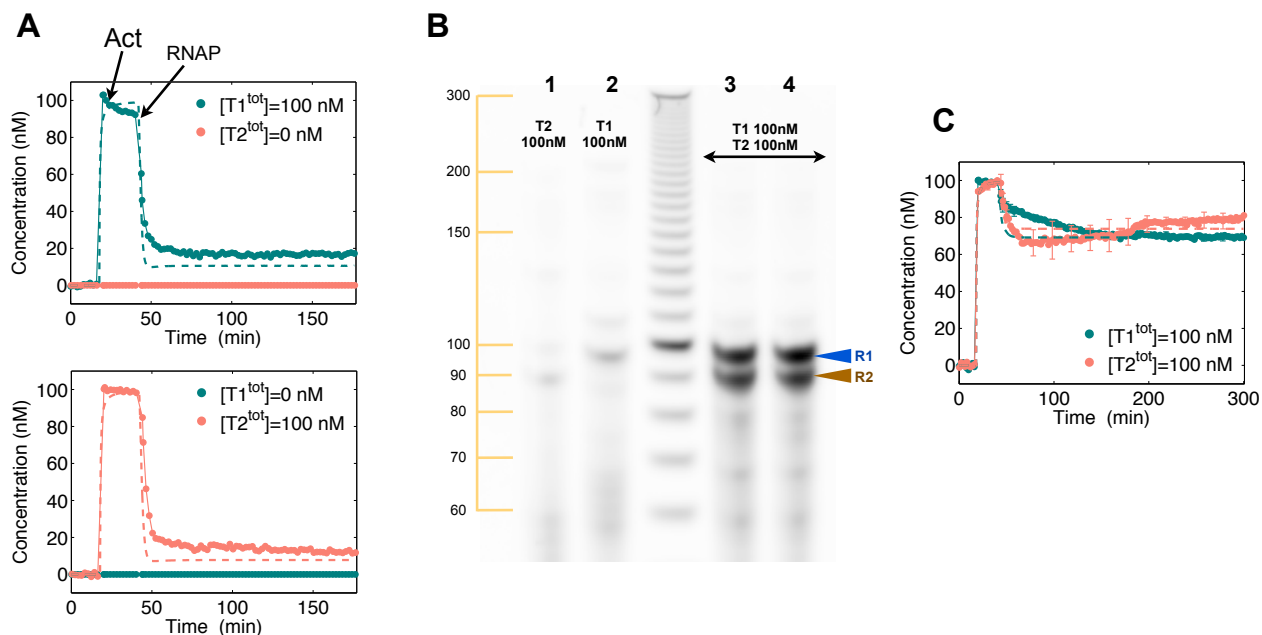


Figure S2: A. Experimental data showing the isolated active genelet concentrations as a function of time: the self-inhibition reaction turns the switches off, and the RNA concentration in solution is negligible, as verified in the gel electrophoresis data in panel B, lanes 1 and 2 (samples taken at steady-state after 2 h). Dashed lines represent numerical trajectories of equations (5), using the fitted parameters in Table S2. B. Denaturing gel image: lanes 1 and 2 show that the switches in isolation self-inhibit and no significant transcription is measured. Lanes 3 and 4 show the total RNA amount in samples from the experiment shown at panel C, taken at steady-state after 2 h. When the genelets are in stoichiometric amount, their flow rates are already balanced and there is only moderate self-inhibition.

total template ratio) versus the steady-state one: we find that the system behaves symmetrically and the steady-state ratio is close to one across all the initial ratios. Therefore, given open loop transcription rates that differ across a factor of 1–3, these results suggest that the system robustly matches the flux of  $R_1$  and  $R_2$ .

### 1.6.3 Flux adaptation

If the concentration of  $[T_i^{tot}]$  and  $[A_i^{tot}]$  is changed over time, the steady-state concentration of active genelets adjusts as shown in Figure S4 A and B. Samples from this set of experiments were analyzed using a denaturing gel: the results are shown in Figure S4 C and D (corresponding to the traces in Figure S4 A and B, respectively) and show the total RNA amount in solution and that  $[R_1^{tot}] \approx [R_2^{tot}]$ , as desired (Figure S4 E and F). The RNA concentrations were estimated using the DNA ladder as a reference. We are aware that this method may result in inaccurate absolute concentration estimates for RNA: however, our objective here is to compare the evolution over time of the relative RNA concentrations. Thus, inaccuracy in the determination of the absolute amount of RNA produced does not affect the measured outcome of our experiments. The adjustment of genelet activity becomes progressively slower over time: the third round of adaptation is consistently slower than the previous two. We attribute this slower adaptation to various phenomena: 1) Decrease of activity of enzymes over time; 2) Accumulation of incomplete degradation products from RNase H hydrolyzation of RNA in RNA-DNA hybrids: these products can be up to 7–8 bases long, and may interfere with the desired inhibition pathways; 3) Abortive transcription of RNA, which could also potentially bind to regulatory domains of DNA activators. Our hypothesis of accumulation of short products over time is validated by the gels shown in Figure S4 C and D (below 60 bases, part of the gel that is not shown, a similar smear is visible).

### 1.6.4 Data fitting

We derived a system of ordinary differential equations (ODEs) starting from mass action kinetics, as described in Section 2.2. The ODE system was numerically fitted using MATLAB (The MathWorks) to fluorescence data in Figures S2 and S3. Only a subset of the parameters was fit using the MATLAB `fmincon` routine. We fit the total RNA polymerase and RNase H concentrations and the rates  $k_{T_i A_i}$ ,  $k_{T_i A_i R_i}$ ,  $k_{A_i R_i}$ ,  $k_{R_1 R_2}$ ,  $k_{R_i T_j}$ , and the parameters  $k_{catON_{ii}}$  and  $k_{catH_{ij}}$ . This specific subset of parameters was chosen because experimental outcomes are chiefly affected by branch migration rates (which are tunable by design of the toehold lengths), enzyme concentration, and enzyme catalytic rates. The concentration and composition of the transcription enzyme mix for the T7 Megashortscript kit are not disclosed by Ambion, but available literature suggests that additional enzymes, such as pyrophosphatase, are present in the mix, Milburn et al. [U. S. Patent 5256555, 1993]. We neglected reactions associated with the possibly unknown amount of pyrophosphatase in the mix. The concentration of RNase H is also not disclosed by Ambion; we did not run separate experiments to fit exclusively the degradation rate parameters. A table reporting all the parameters is in Section 2, Tables S1 and S2.



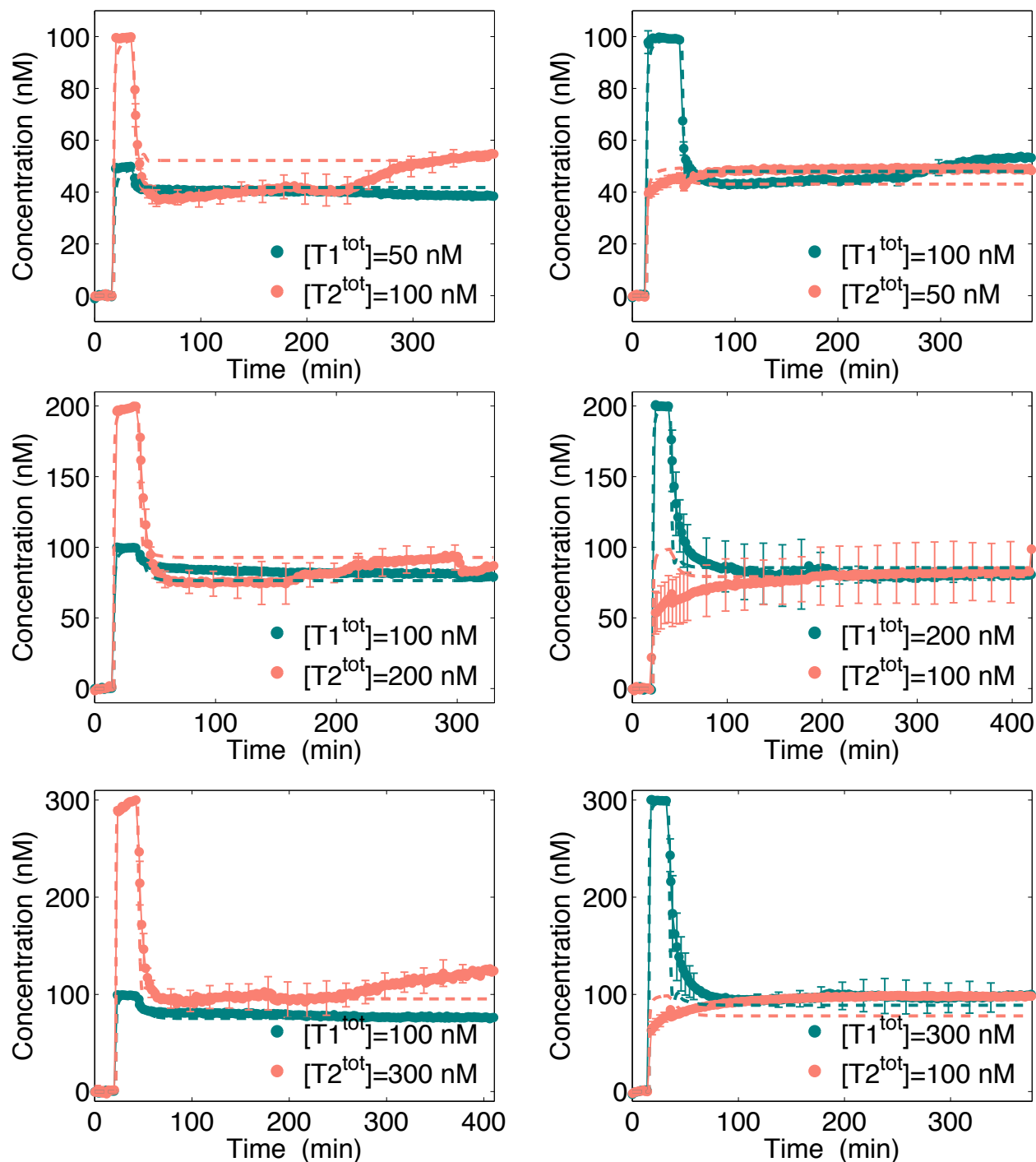


Figure S3: Concentration of active genelets over time at different total templates concentration. The concentration of activators is always stoichiometric to the amount of corresponding template. Dashed lines in all the figures correspond to numerical simulations for model (5), using the parameters in Table S2.

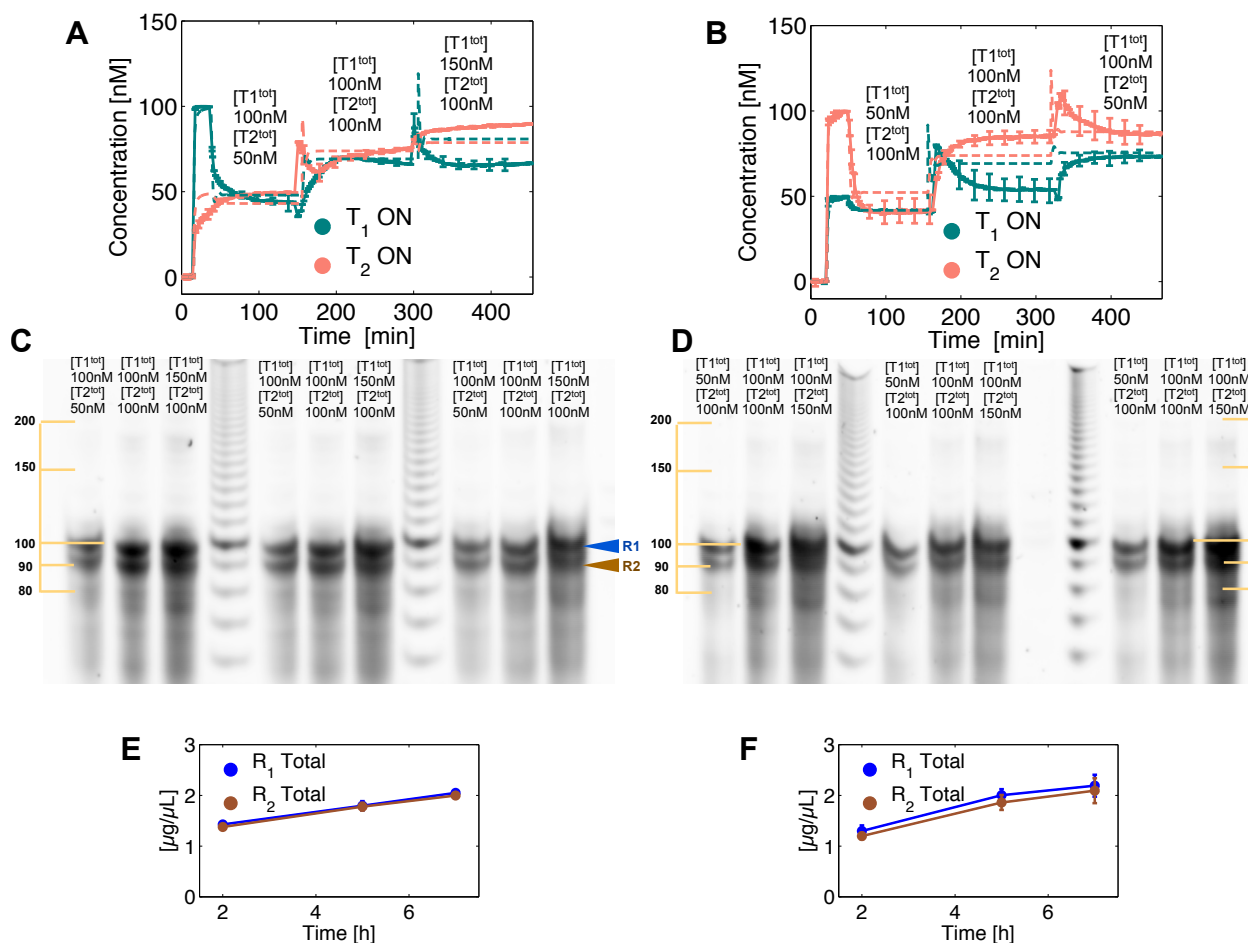
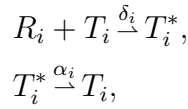


Figure S4: A and B. Fluorescent traces showing the adaptation of the active fraction of genelets, when the total amount of templates is varied over time. C and D. Samples from the experiments shown in panels A and B, respectively, were analyzed with gel electrophoresis. E and F show the concentrations of RNA species, estimated from the gel samples.

## 2 Modeling and numerical analysis: two-gene flux matching system

### 2.1 Simple model system: derivation of nullclines and rate matching conditions

We consider a system composed of two generating species  $T_1$  and  $T_2$ , whose products  $R_1$  and  $R_2$  interact to form a complex  $P = R_1 \cdot R_2$ . We introduce negative autoregulation to minimize the concentration of product that is not used to form the output complex (Figure S5). Free molecules of  $R_i$ ,  $i = 1, 2$ , bind to active  $T_i$ , thereby inactivating it:



where  $T_i^*$  is an inactive complex. We assume that  $T_i^{tot} = T_i + T_i^*$ , and that  $T_i^*$  naturally reverts to its active state with a first-order rate  $\alpha_i$ . The total amount of  $R_i$  is  $[R_i^{tot}] = [R_i] + [T_i^*] + [P]$ . The corresponding differential equations are:

$$\begin{aligned} \frac{d[T_i]}{dt} &= \alpha_i ([T_i^{tot}] - [T_i]) - \delta_i [R_i][T_i], \\ \frac{d[R_i]}{dt} &= \beta_i [T_i] - k [R_i][R_j] - \delta_i [R_i][T_i]. \end{aligned} \quad (1)$$

For illustrative purposes, these differential equations are solved numerically. The parameters chosen are:  $\alpha_1 = \alpha_2 = 3 \cdot 10^{-4}$  /s,  $\beta_1 = \beta_2 = 0.01$  /s,  $\delta_1 = \delta_2 = 5 \cdot 10^2$  /M/s, and  $k = 2 \cdot 10^3$  /M/s. An imbalance in the production rates of  $R_1$  and  $R_2$  is created by setting  $[T_1](0) = [T_1^{tot}] = 100$  nM and  $[T_2](0) = [T_2^{tot}] = 200$  nM, while  $[R_1](0) = [R_2](0) = 0$ . The overall result of this feedback interconnection is that the mismatch in the flow rate of  $R_1$  and  $R_2$  is reduced, as shown in Figure S6. The flow rate is defined as the derivative of  $[R_i^{tot}]$ . The flow rate mismatch is defined as the absolute value of the difference between the two flows. The effect of changing the feedback strength, for simplicity chosen as  $\delta_1 = \delta_2$ , is shown in Figure S7: the figure shows the mean active fraction of  $[T_i]$  and the mean flow mismatch over a trajectory simulated for 10 hours. We show the mean over the last hour of the simulation, rather than steady-state values.

It is possible to examine the nullclines relating  $T_1$  and  $T_2$ , and find the equilibria  $\bar{T}_1$  and  $\bar{T}_2$  as intersection of these nullclines:

$$\begin{aligned} \dot{T}_i = 0 &\implies R_i = \frac{\alpha_i(T_i^{tot} - T_i)}{\delta_i T_i}, \\ \dot{R}_i = 0 &\implies R_i = \frac{\beta_i T_i}{k R_j + \delta_i T_i}. \end{aligned}$$

To simplify the derivation, we set  $\delta_1 = \delta_2 = \delta$ ,  $\beta_1 = \beta_2 = \beta$ ,  $\alpha_1 = \alpha_2 = \alpha$ . Equating the two expressions for  $R_i$ , we get the following equations (for  $i = 1, 2$  and  $j = 1, 2$ ):

$$\left(\frac{\alpha}{\delta}\right)^2 k \left(\frac{T_i^{tot} - T_i}{T_i}\right) \left(\frac{T_j^{tot} - T_j}{T_j}\right) + \alpha(T_i^{tot} - T_i) - \beta T_i = 0.$$

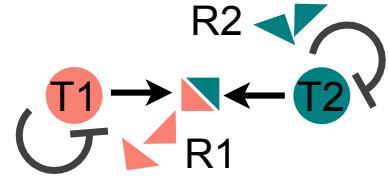


Figure S5: Our two-gene negative feedback architecture

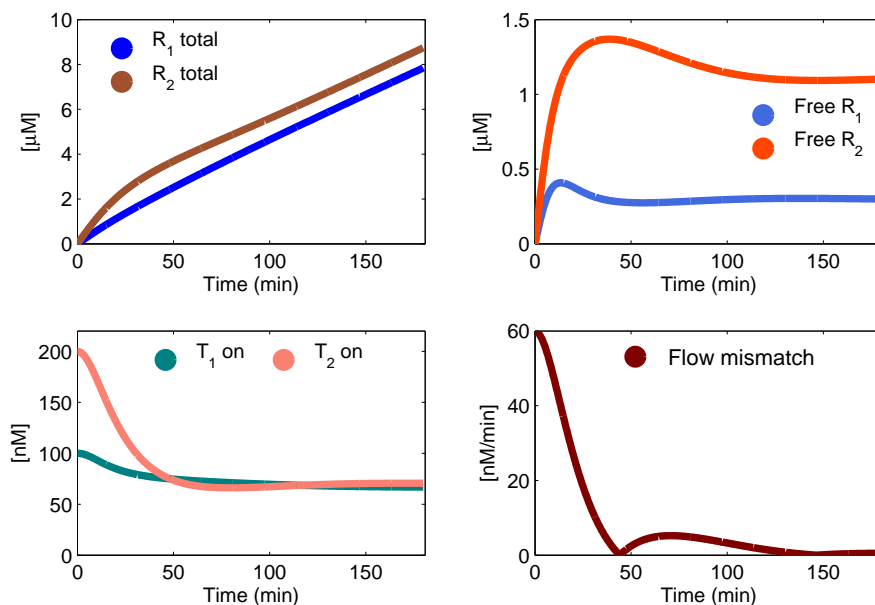


Figure S6: Numerical simulation showing the solution to the two-gene negative feedback architecture for flux matching modeled with equations (1). The flow mismatch between  $R_1$  and  $R_2$  is shown in the bottom-right panel.

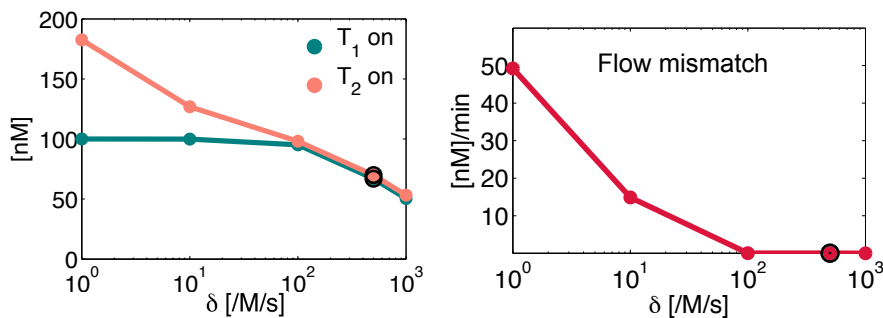


Figure S7: Numerical simulation showing genelet activity and mismatch over a range of values for the negative feedback parameter  $\delta$ .

We can find an expression of the nullclines by introducing a change of variables  $u = \left(\frac{T_1^{tot} - T_1}{T_1}\right)$  and  $v = \left(\frac{T_2^{tot} - T_2}{T_2}\right)$ , and defining  $\phi_1 = \psi_1 = \left(\frac{\alpha}{\delta}\right)^2 k$ ,  $\phi_2 = \alpha T_1^{tot}$ ,  $\psi_2 = \alpha T_2^{tot}$ ,  $\phi_3 = \beta T_2^{tot}$ , and finally  $\psi_3 = \beta T_1^{tot}$ :

$$u^2(\phi_1 v) + u(\phi_1 v + \phi_2 - \phi_3 \frac{1}{1+v}) - \phi_3 \frac{1}{1+v} = 0, \quad (2)$$

$$v^2(\psi_1 u) + v(\phi_1 u + \psi_2 - \psi_3 \frac{1}{1+u}) - \psi_3 \frac{1}{1+u} = 0. \quad (3)$$

The roots of the equations above represent the nullclines of the system. Because all the parameters in these equations are positive, there is always a single root. The nullclines are numerically solved, for varying  $\delta$ , in Figure S8.

A condition for flow matching at steady-state can be derived as follows:

$$\begin{aligned} \dot{R}_1 - \dot{R}_2 &= 0, \\ \beta_1 T_1 - \delta_1 T_1 R_1 &= \beta_2 T_2 - \delta_2 T_2 R_2. \end{aligned}$$

Substituting the expressions for  $R_1$  and  $R_2$  that can be derived by setting  $\dot{T}_1 = 0 = \dot{T}_2$ , we get:

$$\beta_1 \bar{T}_1 - \alpha_1 (T_1^{tot} - \bar{T}_1) = \beta_2 \bar{T}_2 - \alpha_2 (T_2^{tot} - \bar{T}_2).$$

Taking  $\alpha_1 = \alpha_2 = \alpha$ ,  $\beta_1 = \beta_2 = \beta$  we get:

$$\bar{T}_2 = \bar{T}_1 + \frac{\alpha}{\alpha + \beta} (T_2^{tot} - T_1^{tot}). \quad (4)$$

The flow matching condition above is shown in Figure S8, orange line (also shown in the main paper). If  $\beta \gg \alpha$ , i.e., the production of  $R_i$  is much faster than the generating species  $T_i$  inactivation rate, then the condition can be rewritten as:

$$\bar{T}_1 \approx \bar{T}_2.$$

## 2.2 Differential equations modeling the experimental implementation

Based on our design specifications and the resulting molecular interactions, we built a model for the system starting from the list of occurring chemical reactions. The switches  $T_i$  and  $T_j$  can have three possible states: the on state where activator and template are bound and form the complex  $T_i A_i$ ; the off state given by free  $T_i$ ; the off state represented by  $R_j$  bound to  $T_i$  forming  $T_i R_j$ . An off state still allows for *RNAP* weak binding and transcription. Throughout this derivation, the dissociation constants are omitted when assumed to be negligible. It is hypothesized that the concentration of enzymes is considerably lower than that of the DNA molecules, allowing the classical steady-state assumption for Michaelis-Menten kinetics.

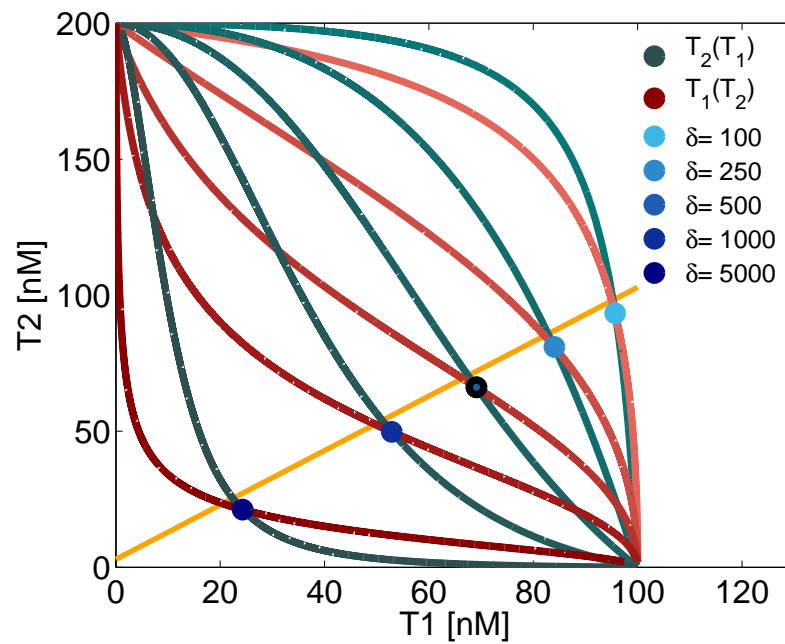
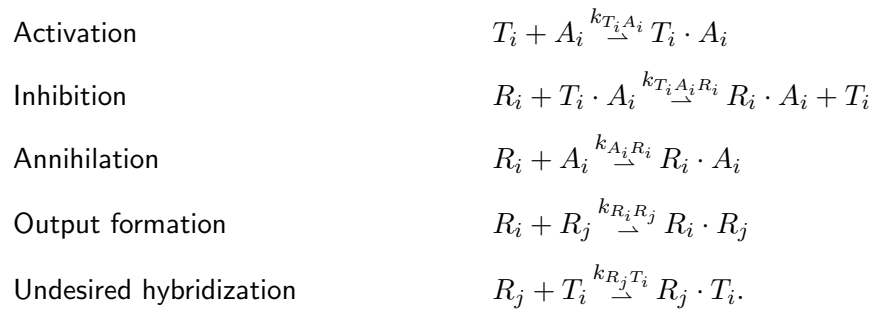
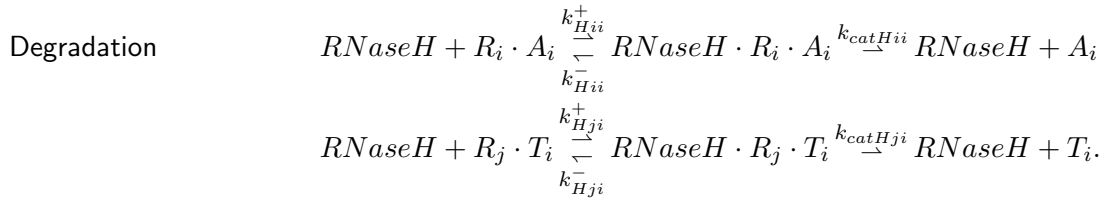
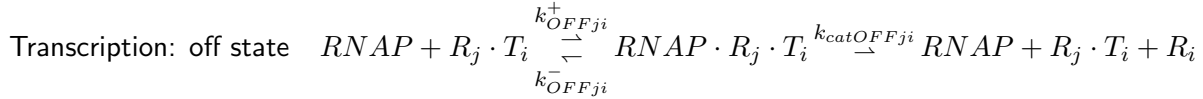
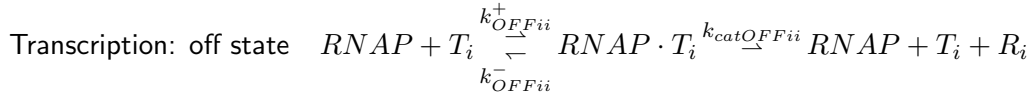
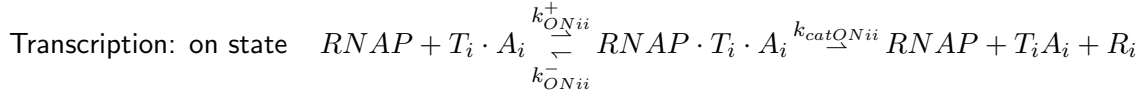


Figure S8: Nullclines computed for different values of negative feedback rate  $\delta$ , and flux matching condition (orange)

Branch migration and hybridization reactions among nucleic acids are, for  $i \in \{1, 2\}$ ,  $j \in \{2, 1\}$ :



The enzymatic reactions are, for  $i \in \{1, 2\}$ ,  $j \in \{2, 1\}$ :



Using the law of mass action, we derive the following ODEs:

$$\begin{aligned} \frac{d}{dt}[T_i] &= -k_{T_i A_i}[T_i][A_i] + k_{T_i A_i R_i}[R_i][T_i \cdot A_i] - k_{R_j T_i}[R_j][T_i] + k_{catHji}[RNaseH \cdot R_j \cdot T_i], \\ \frac{d}{dt}[A_i] &= -k_{T_i A_i}[T_i][A_i] - k_{A_i R_i}[R_i][A_i] + k_{catHii}[RNaseH \cdot R_i \cdot A_i], \\ \frac{d}{dt}[R_i] &= -k_{R_i R_j}[R_i][R_j] - k_{T_i A_i R_i}[R_i][T_i \cdot A_i] - k_{R_i T_j}[R_i][T_j] - k_{A_i R_i}[R_i][A_i] \\ &\quad + k_{catONii}[RNAP \cdot T_i \cdot A_i] + k_{catOFFii}[RNAP \cdot T_i] + k_{catOFFji}[RNAP \cdot R_j \cdot T_i], \\ \frac{d}{dt}[R_i \cdot R_j] &= +k_{R_i R_j}[R_i][R_j], \\ \frac{d}{dt}[R_j \cdot T_i] &= +k_{R_j T_i}[R_j][T_i] - k_{catHji}[RNaseH \cdot R_j \cdot T_i]. \end{aligned} \tag{5}$$

The molecular complexes appearing at the right-hand side of these equations can be expressed using mass conservation:

$$[T_i \cdot A_i] = [T_i^{tot}] - [T_i] - [R_j \cdot T_i], \quad [R_i \cdot A_i] = [A_i^{tot}] - [A_i] - [T_i \cdot A_i].$$

We assume that binding of enzymes to their substrate is faster than the subsequent catalytic step, and that the substrate concentration is larger than the total amount of enzyme. These assumptions allow us to use the standard Michaelis-Menten quasi-steady-state expressions. The Michaelis-Menten coefficients can be immediately defined; for instance, for the ON state of the template, define:  $k_{MONii} = \frac{k_{ONii}^- + k_{catONii}}{k_{ONii}^+}$ . Then we find:

$$\begin{aligned} [RNAP^{tot}] &= [RNAP] \left( 1 + \frac{[T_1 \cdot A_1]}{k_{MON11}} + \frac{[T_1]}{k_{MOFF11}} + \frac{[T_2 \cdot A_2]}{k_{MON22}} + \frac{[T_2]}{k_{MOFF22}} + \frac{[R_2 \cdot T_1]}{k_{MOFF21}} + \frac{[R_1 \cdot T_2]}{k_{MOFF12}} \right), \\ [RNaseH^{tot}] &= [RNaseH] \left( 1 + \frac{[R_1 \cdot A_1]}{k_{MH11}} + \frac{[R_2 \cdot A_2]}{k_{MH22}} + \frac{[R_2 \cdot T_1]}{k_{MH21}} + \frac{[R_1 \cdot T_2]}{k_{MH12}} \right). \end{aligned}$$

We can easily rewrite these equations as  $[RNAP] = \frac{[RNAP^{tot}]}{P}$  and  $[RNaseH] = \frac{[RNaseH^{tot}]}{H}$ , with a straightforward definition of the coefficients  $P$  and  $H$ . Finally:

$$\begin{aligned} [RNAP \cdot T_i \cdot A_i] &= \frac{[RNAP^{tot}] [T_i \cdot A_i]}{P \cdot k_{MONii}}, \\ [RNAP \cdot R_j \cdot T_i] &= \frac{[RNAP^{tot}] [R_j \cdot T_i]}{P \cdot k_{MOFFji}}, \\ [RNAP \cdot T_i] &= \frac{[RNAP^{tot}] [T_i]}{P \cdot k_{MOFFii}}, \\ [RNaseH \cdot R_i \cdot A_i] &= \frac{[RNaseH^{tot}] [R_i \cdot A_i]}{H \cdot k_{MHii}}, \\ [RNaseH \cdot R_j \cdot T_i] &= \frac{[RNaseH^{tot}] [R_j \cdot T_i]}{H \cdot k_{MHji}}, \end{aligned}$$

which can be substituted in equations (5). We note that our numerical fits result in an estimated  $RNAP$  concentration of about 100 nM: thus, in a subset of our experiments the substrate and enzyme concentrations are actually comparable, breaking down one of the assumptions required for a quasi-steady-state approximation. Nevertheless, our model overall captures the system dynamics satisfactorily.

The nonlinear set of equations (5) was solved numerically using MATLAB ode23 routine.

**Preliminary numerical analysis** Prior to designing DNA strands and testing the system with wet lab experiments, we ran numerical simulations using equations (5) using parameters reported in Table S1. These parameters are consistent with those in Kim et al. [2006], which were fitted from data obtained on a transcriptional system with identical promoter/branch migration design specifications and sequence content; thus, we refer the reader to Kim et al. [2006] for an accurate discussion and comparison to other branch migration, transcription, and degradation parameters found in the literature. Figure S9 shows the system trajectories that correspond to zero initial conditions for  $[A_i]$  and  $[R_i]$ , while the complexes  $[T_1 A_1] = [T_1^{tot}] = 100$  nM,  $[T_2 A_2] = [T_2^{tot}] = 50$  nM,  $[A_1^{tot}] = 100$  nM and  $[A_2^{tot}] = 50$  nM. (The simulation first allows for equilibration of all the DNA strands in the absence of enzymes. Only the portion of trajectories after addition of enzymes is shown.) The total concentration of enzymes was assumed to be  $[RNAP^{tot}] = 80$  nM and  $[RNaseH^{tot}] = 8.8$  nM, consistent with typical volumes used in our experiments and with enzyme stock concentrations of about 1–1.25  $\mu$  M Kim and Winfree [2011], Franco et al. [2011]. An example of our numerical simulation results is shown in Figure S9. The behavior of the system proved to be consistent with the traces obtained for the simple model system shown at Figure S6.

**Data fitting results** As already indicated in Section 1.6.4, equations (5) were fitted to all fluorescence data in Figures S2 and S3 simultaneously, using MATLAB routine `fmincon`. Only a subset of the parameters was fit: the total RNA polymerase and RNase H concentrations, and the rates  $k_{T_i A_i}$ ,  $k_{T_i A_i R_i}$ ,  $k_{A_i R_i}$ ,  $k_{R_1 R_2}$ ,  $k_{R_i T_j}$ , and the parameters  $k_{catONii}$  and  $k_{catHij}$ . Table S2 lists the results of the data fit; Table S3 reports the constraints used in the fitting procedure. Our fits indicate that the hybridization and branch migration rates fitting these experiments are higher than what found in Kim et al. [2006], Franco et al. [2011]. In particular, the binding rate of the RNA species is higher than expected; hybridization rates for complementary RNA strands of



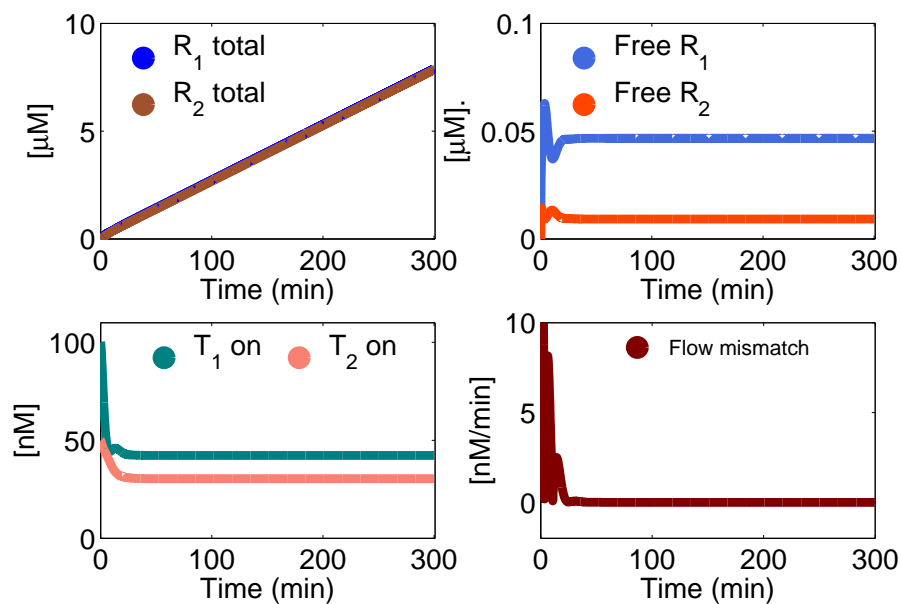


Figure S9: Numerical simulation for equations (5). Parameters are chosen as in Table S1.  $[T_1^{tot}] = [A_1^{tot}] = 100 \text{ nM}$ ,  $[T_2^{tot}] = [A_2^{tot}] = 50 \text{ nM}$ ,  $[RNAP^{tot}] = 80 \text{ nM}$ , and  $[RNaseH^{tot}] = 8.8 \text{ nM}$ . These results are consistent with those of the simple model proposed in equations (1), and analyzed numerically in Figure S6.

Table S1: Preliminary Simulation Parameters for Equations (5)

Units: $[1/M/s]$	Units: $[1/s]$	Units: $[M]$
$k_{T_i A_i} = 4 \cdot 10^4$	$k_{catON_{ii}} = 0.06$	$k_{MON_{ii}} = 250 \cdot 10^{-9}$
$k_{T_i A_i R_i} = 5 \cdot 10^4$	$k_{catOFF_{ii}} = 1 \cdot 10^{-3}$	$k_{MOFF_i} = 1 \cdot 10^{-6}$
$k_{A_i R_i} = 5 \cdot 10^4$	$k_{catOFF_{ij}} = .5 \cdot 10^{-3}$	$k_{MOFF_{ij}} = 1 \cdot 10^{-6}$
$k_{R_i T_j} = 1 \cdot 10^4$	$k_{catH_{ii}} = .1$	$k_{MH_{ii}} = 50 \cdot 10^{-9}$
$k_{R_i R_j} = 1 \cdot 10^6$	$k_{catH_{ji}} = .1$	$k_{MH_{ji}} = 50 \cdot 10^{-9}$
Units: $[M]$	Units: $[M]$	
$[RNAP^{tot}] = 80 \text{ nM}$	$[RNaseH^{tot}] = 8.8 \text{ nM}$	

similar length have (to our knowledge) not been assessed before. The expected concentrations of RNA polymerase and RNase H and their  $k_{cat}$  values are also higher than in previous studies Kim et al. [2006], Franco et al. [2011], where lower hybridization rates were attributed to the presence of incomplete degradation products from RNase H hydrolyzation of DNA/RNA hybrids. These short products, known to have length up to 7–8 bases, may interfere with desired regulatory pathways Kim and Winfree [2011]. Because the activity and efficiency of off-the-shelf enzymes is known to considerably vary from batch to batch Kim and Winfree [2011], it is reasonable to hypothesize that the RNA polymerase and RNase H batches used in this set of experiments had particularly high activity and low occurrence of incomplete transcription/degradation which can slow down other reactions. Indeed, the accumulation of these incomplete products over time may be the reason for slower dynamics observed in our adaptation experiments in Figure S4.

Table S2: Fitted Parameters for (5); other parameters were left unvaried with respect to Table S1

Units: $[1/M/s]$	Units: $[1/s]$
$k_{T_i A_i} = 6.6 \cdot 10^5$	$k_{catON_{11}} = 0.1, k_{catON_{22}} = 0.09$
$k_{T_1 A_1 R_1} = 0.7 \cdot 10^5, k_{T_2 A_2 R_2} = 0.6 \cdot 10^5$	$k_{catH_{ii}} = .09$
$k_{A_1 R_1} = k_{A_2 R_2} = 4.4 \cdot 10^5$	$k_{catH_{21}} = .03, k_{catH_{12}} = .02$
$k_{R_i R_j} = 4.9 \cdot 10^6$	
Units: $[M]$	Units: $[M]$
$[RNAP^{tot}] = 100 \text{ nM}$	$[RNaseH^{tot}] = 20 \text{ nM}$

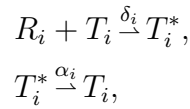
Table S3: Fitting constraints for parameters in Table S2.

Parameter	Lower Bound	Upper Bound
$k_{T_i A_i}$	$10^3$	$5 \cdot 10^5$
$k_{T_i A_i R_i}$	$10^3$	$5 \cdot 10^5$
$k_{A_i R_i}$	$10^3$	$5 \cdot 10^5$
$k_{R_i R_j}$	$10^3$	$5 \cdot 10^5$
$k_{catON_{ii}}$	0.01	0.1
$k_{catH_{ii}}$	0.001	0.1
$[RNAP^{tot}]$	$15 \cdot 10^{-9}$	$100 \cdot 10^{-9}$
$[RNaseH^{tot}]$	$5 \cdot 10^{-9}$	$20 \cdot 10^{-9}$

### 3 Modeling and numerical analysis: Scalability of the negative feedback scheme for flux regulation

#### 3.1 Simple model system

We consider now  $n$  generating species  $T_i$ , outputting interacting products  $R_i$ , and we explore different feedback interconnection topologies. Initial studies on scalability were outlined in Giordano et al. [2013]. ODEs were derived using mass action kinetics and used for numerical simulation of three- and four-component networks. Negative autoregulation is implemented, as for smaller networks, with a self-repression scheme: when an output is in excess relative to the effectively used amount, it down-regulates its own production rate.



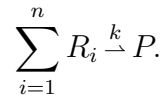
where  $T_i^*$  is an inactive complex. We assume that  $[T_i^{tot}] = [T_i] + [T_i^*]$  and that  $T_i^*$  spontaneously reverts to its active state with a first-order rate  $\alpha_i$ . The corresponding differential equation describing the template dynamics is the same regardless of the topology:

$$\frac{d[T_i]}{dt} = \alpha_i ([T_i^{tot}] - [T_i]) - \delta_i [R_i][T_i], \quad i = 1, \dots, n.$$

Depending on the chosen interaction/binding topology for the products  $R_i$ , we find that the system exhibits different behaviors, as shown in the following sections.

##### 3.1.1 Single product topology

A single product topology occurs when a single complex  $P$  is formed by the simultaneous interaction of all the  $n$  outputs:



The corresponding differential equations are

$$\begin{aligned} \frac{d[R_i]}{dt} &= \beta_i [T_i] - \delta_i [R_i][T_i] - k \prod_{i=1}^n [R_i], \\ \frac{d[P]}{dt} &= k \prod_{i=1}^n [R_i] \end{aligned}$$

and the total amount of  $R_i$  is  $[R_i^{tot}] = [R_i] + [T_i^*] + [P]$ . Figure S10 shows the numerical solutions to the ODEs for  $n = 3$  and  $n = 4$ . Even though the initial total amounts of  $T_i$  are different, the concentration of active  $T_i$  (bottom left panel) gradually decreases and the flow mismatches (namely the differences in absolute value between any two production rates, shown in the bottom right panel) are considerably reduced with a fast time response. We can notice that the response is slower in the case of 4 interconnected species. The quantity of produced  $R_i$  (upper left panel) is of course increasing. With respect to the other topologies, as we will see, the single product topology leads to a much higher amount of free  $R_i$  (upper right panel), which can be considered waste because it is not used in the product formation.

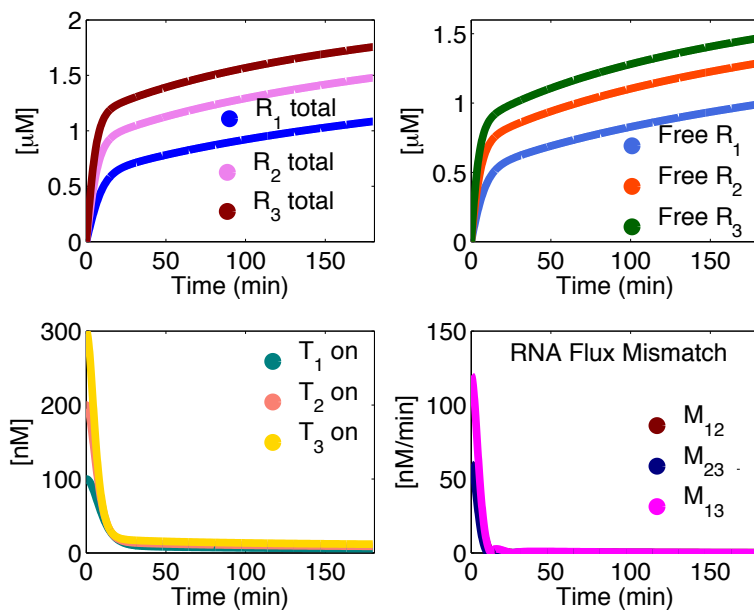
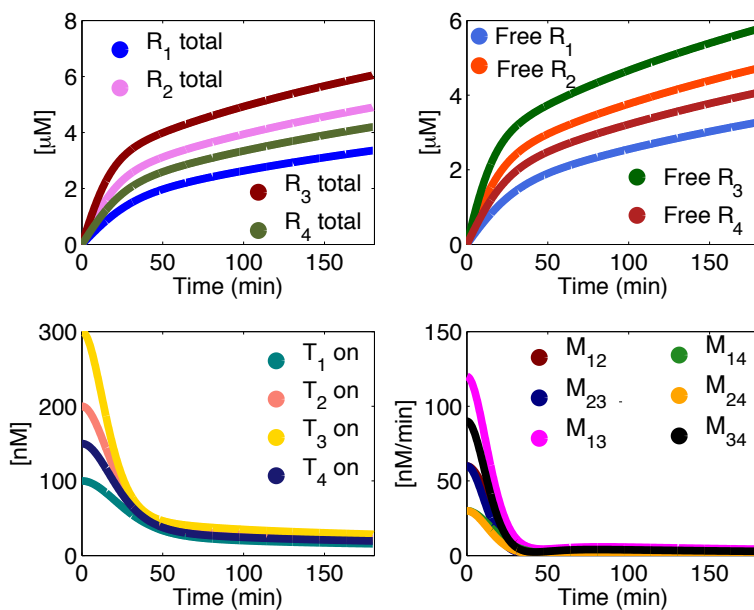
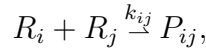
(a) single product,  $n = 3$ (b) single product,  $n = 4$ 

Figure S10: Example traces from numerical simulations: single product topology, negative feed-back scheme.

### 3.1.2 Handshake and neighbor topologies

A network of  $n$  generating species  $T_i$  may be designed to produce different subcomponents, that may later assemble into a larger product. In this scenario, we can take two extreme cases: the neighbor topology, when each output participates in at most two subcomponents, and the handshake topology, when each output participates in  $n - 1$  subcomponents. We thus have the generation of pairwise products  $P_{ij}$ ; in the handshake case  $i, j = 1, \dots, n, j \neq i$ , while in the neighbor case  $i = 1, \dots, n, j = i - 1, i + 1$  and when  $i = 1, i - 1 = n$ , when  $i = n, i + 1 = 1$ , to close the loop. It is worth noticing that, in the case  $n = 3$ , the two topologies coincide. The reactions corresponding to product generation are



which lead to the following ODEs:

$$\begin{aligned} \frac{d[R_i]}{dt} &= \beta_i [T_i] - \delta_i [R_i][T_i] - \sum_j k_{ij} [R_i][R_j], \\ \frac{d[P_{ij}]}{dt} &= k_{ij} [R_i][R_j]. \end{aligned}$$

The total amount of  $R_i$  is  $[R_i^{tot}] = [R_i] + [T_i^*] + \sum_j [P_{ij}]$ . Figure S11 shows the numerical solutions to the ODEs for  $n = 3$ , and for  $n = 4$  in the handshake connection case. As for the single product topology, even though we initially have different total amounts of active  $T_i$ , the concentration of active  $T_i$  decreases and the flux mismatches are considerably reduced with a fast time response. Although the quantity of produced  $R_i$  is increasing, the feedback control reduces and keeps bounded the amount of free  $R_i$ , which can be considered waste.

### 3.1.3 Parameters

The parameters chosen in our simulations are:  $k_{ij} = 2 \cdot 10^3$  /M/s for the handshake/neighbor topology and  $k = 6 \cdot 10^3$  /M/s for the single product topology,  $\delta_i = 5 \cdot 10^3$  /M/s,  $\alpha_i = 3 \cdot 10^{-4}$  /s,  $\beta_i = 1 \cdot 10^{-2}$  /s,  $[T_1^{tot}] = 100$  nM,  $[T_2^{tot}] = 200$  nM,  $[T_3^{tot}] = 300$  nM,  $[T_4^{tot}] = 150$  nM. An imbalance in the production rates of  $R_i$  is created by setting  $[T_i](0) = [T_i^{tot}]$ , while  $[R_i](0) = 0$ .

### 3.1.4 Performance overview of the different topologies as a function of key parameters

We numerically explored the behavior of the different network topologies for  $n = 4$  as a function of the feedback parameter  $\delta$  and of the rate of activation  $\alpha$ . Figures S12, S13 and S14 show the network response in terms of active percentage of  $T_i$  ( $[T_i]/[T_i^{tot}] \cdot 100$ ), flow mismatch (computed as in the previous cases) and response time (defined as the time it takes for the active  $T_i$  trajectory to go from  $[T_i(0)] - 10\% \Delta$  to  $[T_i(0)] - 90\% \Delta$ , where  $\Delta$  is the difference between its initial value  $[T_i(0)]$  and its steady state value). We solved the differential equations for a time span of 10 hours and averaged the trajectories for active  $T_i$  and for the computed mismatch over the last simulation hour.  $\delta$  varies logarithmically from a tenth to a thousand times its nominal value;  $\alpha$  varies from a hundredth to five times its nominal value. In each figure, pink squares mark the nominal behavior of the system (all parameters are identical to those listed in Section 3.1.3).

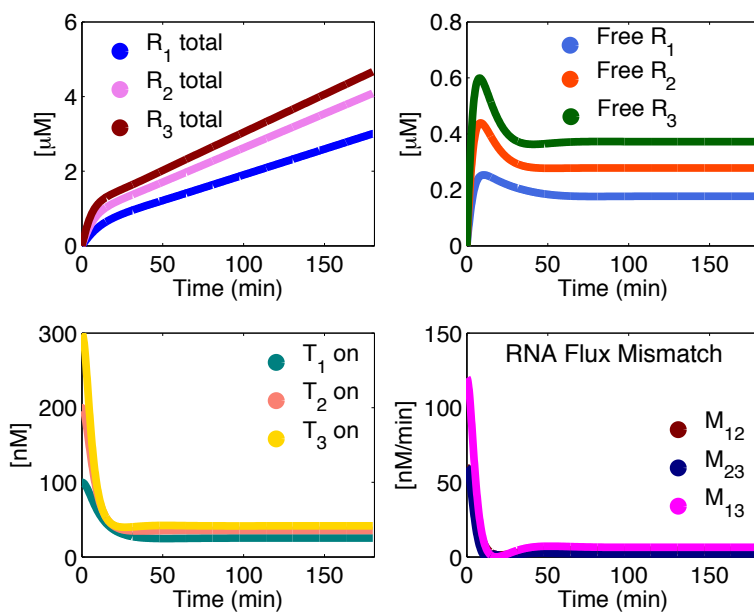
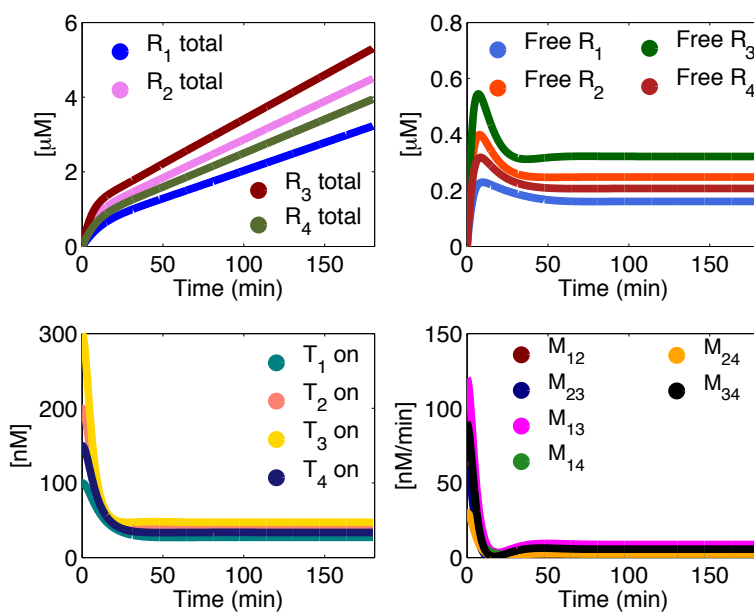
(a) handshake/neighbor,  $n = 3$ (b) handshake,  $n = 4$ 

Figure S11: Example traces from numerical simulations: handshake/neighbor topologies, negative feedback scheme.

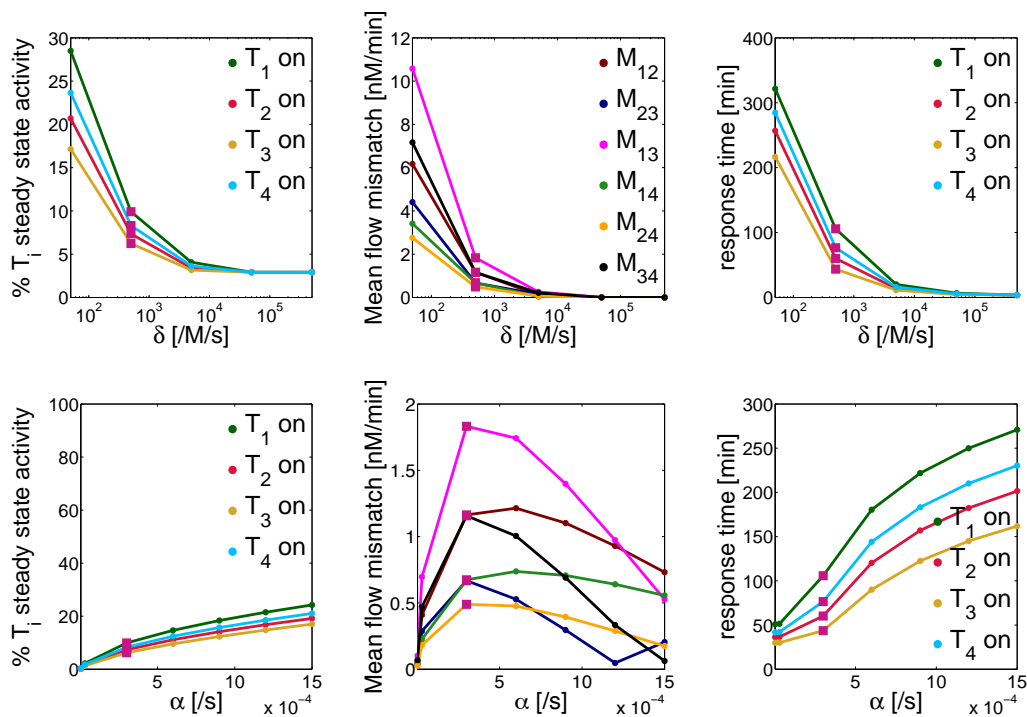


Figure S12: Simulations for the negative feedback, single product topology: parameter sensitivity analysis.

In all network topologies, a large negative feedback parameter  $\delta$  yields a lower mismatch and decreases the response time; however, large  $\delta$  clearly reduces the steady state activity of  $T_i$ . In the handshake and neighbor topologies, a larger value of the spontaneous reactivation parameter  $\alpha$  yields higher  $T_i$  steady state activity, a larger mismatch, and a shorter response time. On the contrary, in the single product topology larger  $\alpha$ , despite yielding higher  $T_i$  steady state activity, dramatically increases the response time, while the mismatch does not monotonically increase.



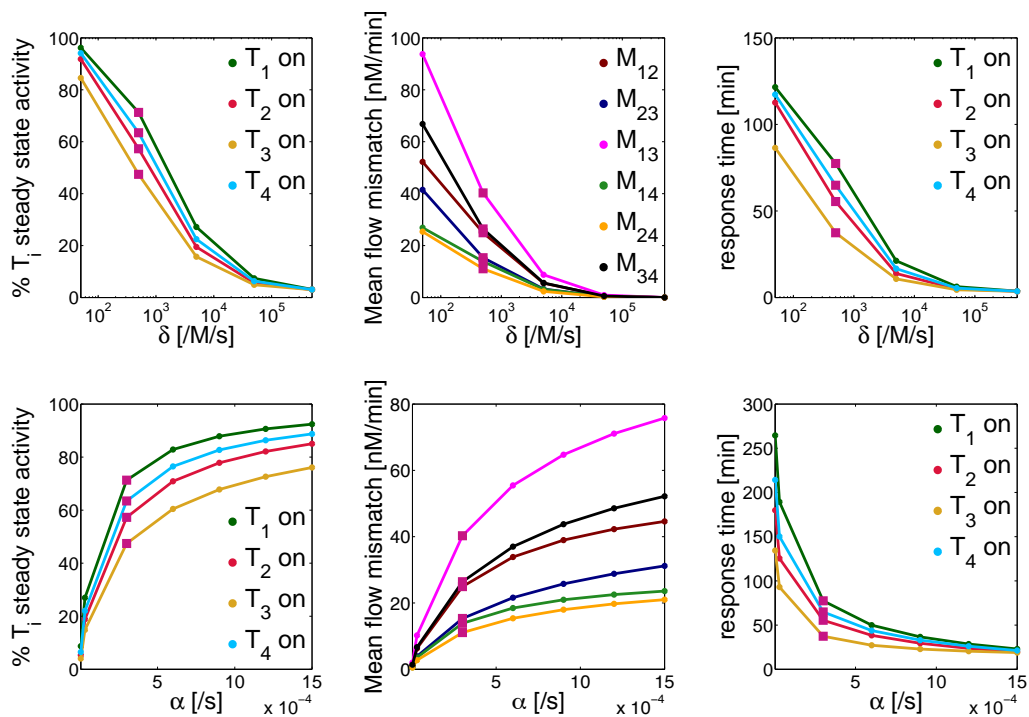


Figure S13: Simulations for the negative feedback, handshake topology: parameter sensitivity analysis.

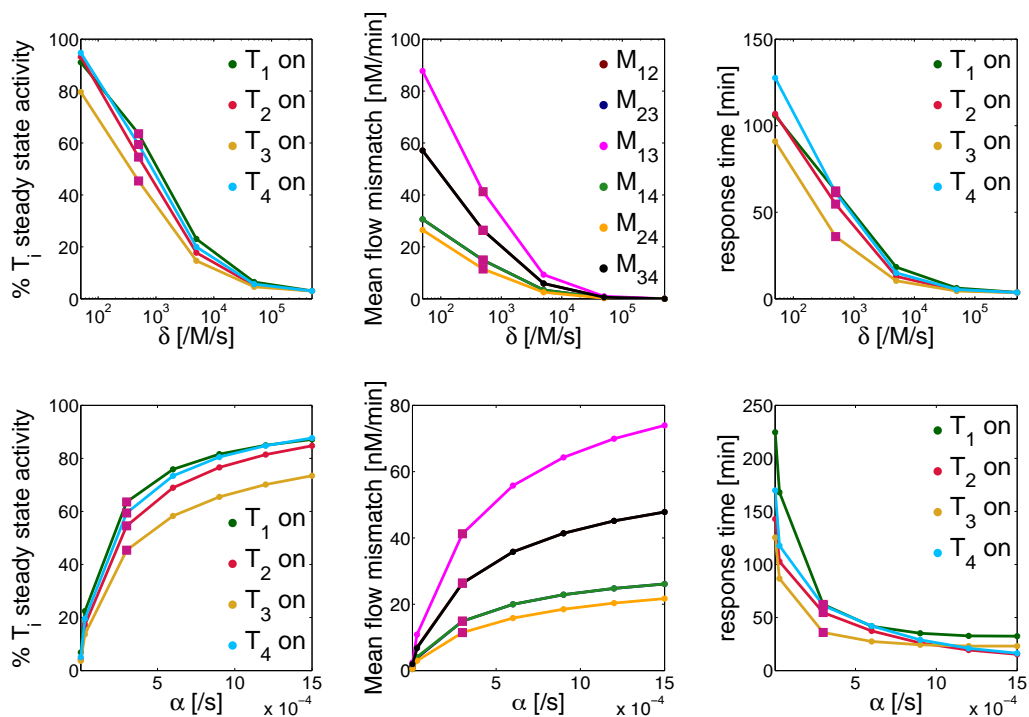


Figure S14: Simulations for the negative feedback, neighbor topology: parameter sensitivity analysis.

## 4 Positive feedback architecture for a two-gene system. Modeling and a viable experimental implementation

### 4.1 Simple model system: derivation of nullclines and rate matching conditions

As done for the negative feedback architecture, we consider a system composed of two generating species  $T_1$  and  $T_2$ , whose products  $R_1$  and  $R_2$  interact to form a complex  $P = R_1 \cdot R_2$ . We devise a positive feedback interconnection where product in excess upregulates the product in shortage (Figure S15). Free (and thus, in excess) molecules of  $R_i$  bind to inactive  $T_j$  and activate it:

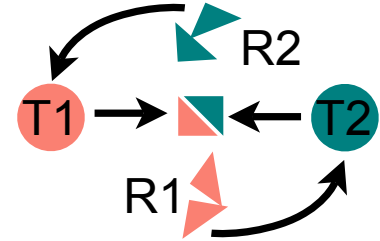
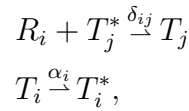


Figure S15: Our two-gene positive feedback architecture

where again  $T_i^*$  is an inactive complex and  $[T_i^{tot}] = [T_i] + [T_i^*]$ . The total amount of  $R_i$  is  $[R_i^{tot}] = [R_i] + [T_j] + [P]$ . We now assume that  $T_i$  naturally reverts to its inactive state with rate  $\alpha_i$ . The corresponding differential equations are

$$\begin{aligned} \frac{d[T_i]}{dt} &= -\alpha_i [T_i] + \delta_{ji} [R_j] ([T_i^{tot}] - [T_i]), \\ \frac{d[R_i]}{dt} &= \beta_i [T_i] - k [R_i] [R_j] - \delta_{ij} [R_i] ([T_j^{tot}] - [T_j]). \end{aligned} \quad (6)$$

This system was initially considered in Franco [2012]. The above differential equations were solved numerically. The parameters were chosen for illustrative purposes as  $\alpha_1 = \alpha_2 = 3 \cdot 10^{-4}$  /s,  $\beta_1 = \beta_2 = 0.01$  /s,  $\delta_1 = \delta_2 = 5 \cdot 10^2$  /M/s, and  $k = 2 \cdot 10^3$  /M/s. The total amount of templates was chosen as  $[T_1^{tot}] = 100$  nM,  $[T_2^{tot}] = 200$  nM. The initial conditions of active  $[T_i]$  are set as  $[T_1](0) = 10$  nM and  $[T_2](0) = 160$  nM, while  $[R_1](0) = [R_2](0) = 0$ . Example traces are shown in Figure S16 (a modified version of this figure is also in the main paper). Each product's flux rate is defined again as the derivative of  $[R_i^{tot}]$ . The flux mismatch is defined as the absolute value of the difference between the two flux rates. The effect of changing the feedback strength, where for simplicity  $\delta_1 = \delta_2$ , is shown in Figure S16 B and C, which plots the active fraction of  $[T_i]$  and the flux mismatch averaged over the last hour of a 10 hours simulation. The right panel in Figure S16 seems to indicate that the flux mismatch of the two circuits is minimized for a certain range of  $\delta$  around the nominal value of  $\delta = 5 \cdot 10^2$ .

The nullclines of the system in the  $T_1$ - $T_2$  space can be calculated as done for the negative feedback design. Taking equations (6), we find:

$$\begin{aligned} \dot{T}_j = 0 &\implies R_i = \frac{\alpha_j T_j}{\delta_{ij} (T_j^{tot} - T_j)}, \\ \dot{R}_i = 0 &\implies R_i = \frac{\beta_i T_i}{k R_j + \delta_{ij} (T_j^{tot} - T_j)}. \end{aligned}$$

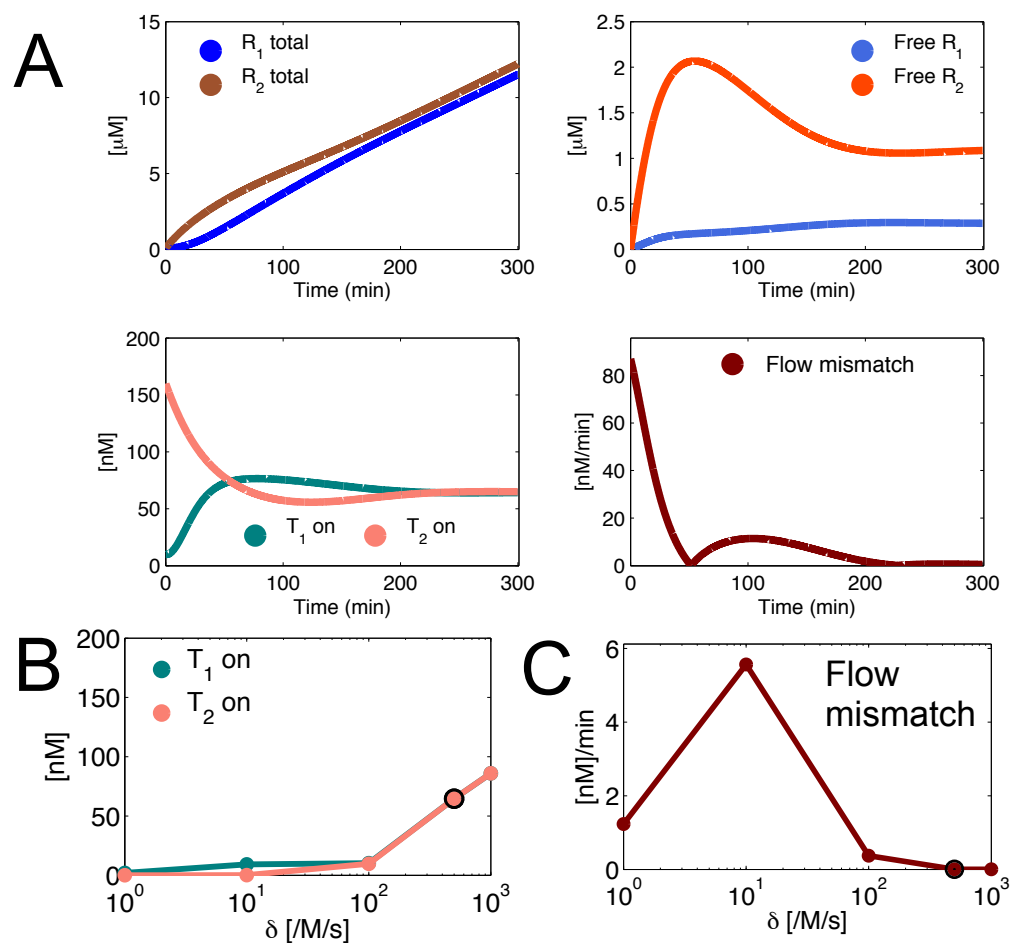


Figure S16: A: Example numerical simulation showing the time evolution of the source species in the positive feedback architecture (Figure S15 modeled with equations (6)). B: Active concentration of source species as a function of the positive feedback rate  $\delta$ . C: Flow mismatch between  $R_1$  and  $R_2$  as a function of  $\delta$ . Dark circles indicate the value of  $\delta$  used in panel A.

To simplify the derivation, we set  $\delta_{12} = \delta_{21} = \delta$ ,  $\beta_1 = \beta_2 = \beta$ ,  $\alpha_1 = \alpha_2 = \alpha$ . Equating the two expressions for  $R_i$ , we get the following equations (for  $i = 1, 2$  and  $j = 1, 2$ ):

$$\left(\frac{\alpha}{\delta}\right)^2 k \left(\frac{T_i}{T_i^{tot} - T_i}\right) \left(\frac{T_j}{T_j^{tot} - T_j}\right) + \alpha T_i - \beta T_j = 0. \quad (7)$$

We can find an expression of the nullclines by introducing a change of variables  $z = \left(\frac{T_1}{T_1^{tot} - T_1}\right)$  and  $w = \left(\frac{T_2}{T_2^{tot} - T_2}\right)$ , and defining  $\phi_1 = \psi_1 = \left(\frac{\alpha}{\delta}\right)^2 k$ ,  $\phi_2 = \alpha T_1^{tot}$ ,  $\psi_2 = \alpha T_2^{tot}$ ,  $\phi_3 = \beta T_2^{tot}$ , and finally  $\psi_3 = \beta T_1^{tot}$ :

$$z^2(\phi_1 w) + z(\phi_1 w + \phi_2 - \phi_3 \frac{w}{1+w}) - \phi_3 \frac{w}{1+w} = 0, \quad (8)$$

$$w^2(\psi_1 z) + w(\phi_1 z + \psi_2 - \psi_3 \frac{z}{1+z}) - \psi_3 \frac{z}{1+z} = 0. \quad (9)$$

The roots of the equations above represent the nullclines of the system. Because all the parameters in these equations are positive, there is always a single root. The nullclines are numerically solved, for varying  $\delta$ , in Figure S17. A condition for flow matching at steady-state can be derived as follows:

$$\begin{aligned} \dot{R}_1 - \dot{R}_2 &= 0, \\ \beta_1 T_1 - \delta_{21} R_1 (T_2^{tot} - T_2) &= \beta_2 T_2 - \delta_{12} R_2 (T_1^{tot} - T_1). \end{aligned}$$

Substituting the expressions for  $R_1$  and  $R_2$  that can be derived by setting  $\dot{T}_1 = 0 = \dot{T}_2$ , we get:

$$\beta_1 \bar{T}_1 - \frac{\delta_{21}}{\delta_{12}} \alpha_2 \bar{T}_2 = \beta_2 \bar{T}_2 - \frac{\delta_{12}}{\delta_{21}} \alpha_1 \bar{T}_1.$$

Taking  $\alpha_1 = \alpha_2 = \alpha$ ,  $\beta_1 = \beta_2 = \beta$ , and  $\delta_{12} = \delta_{21} = \delta$  we get:

$$\bar{T}_2 = \bar{T}_1. \quad (10)$$

This flow matching condition is shown in Figure S17 in the red dashed line. Decreasing  $\alpha$  (inactivation rate for the generating species) or increasing  $\delta$  (speed of the positive feedback), with respect to the nominal values chosen here, causes the equilibrium of the system to be pushed toward the upper right corner of Figure S17. Moreover, when decreasing  $\alpha$  or increasing  $\delta$  the system reaches equilibrium on a timescale in the order of several dozens of hours. Explicit tradeoffs on the effects of  $\alpha$  and  $\delta$  may be found by further analysis on the nullclines and on the locus of equilibria in equation (7).

## 4.2 A possible experimental implementation of a two-gene positive feedback scheme

The experimental implementation of our positive feedback scheme using transcriptional networks presents several challenges. Here we present its general idea. A viable strand design scheme is in

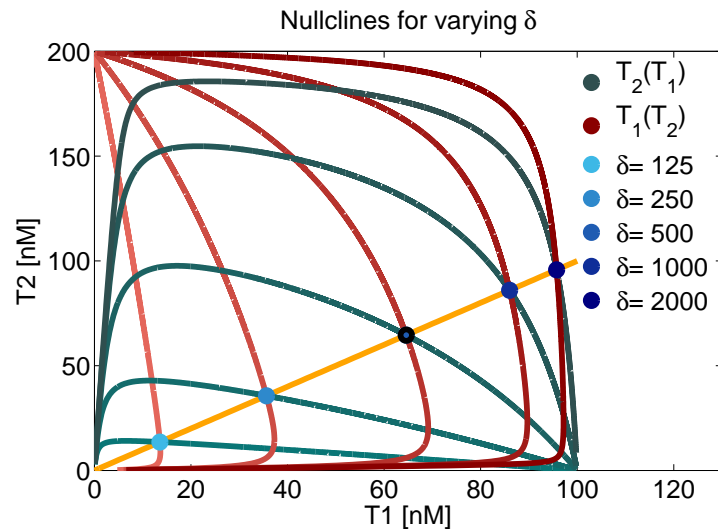


Figure S17: Numerical simulation: nullclines of the positive feedback scheme (6) in the  $T_1$ - $T_2$  plane, calculated for different values of  $\delta$  finding the roots of equations (8) and (9). The equilibrium corresponding to the set of nominal parameters (trajectories in Figure S16 A) is circled in black. The flow matching condition (10) is shown in the orange line. The flow matching condition is satisfied by the equilibria  $\bar{T}_1$  and  $\bar{T}_2$  for  $\delta = 5 \cdot 10^3$ .

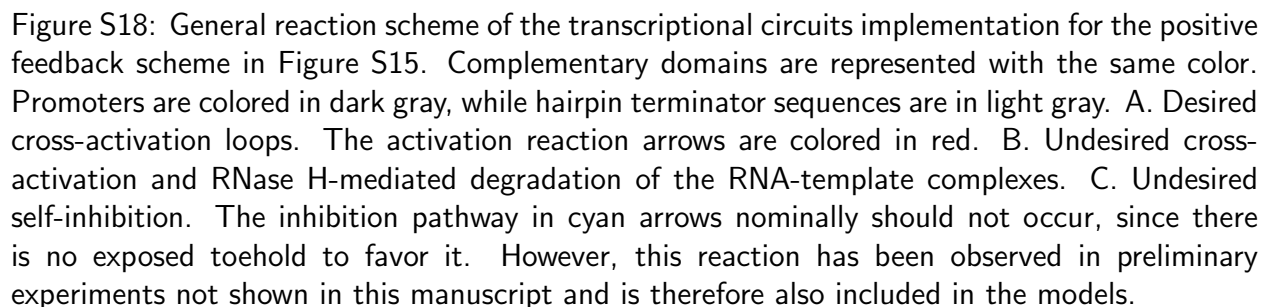
Figure S18 A. Both genelets are constitutively inhibited by a DNA inhibitor  $I_i$ . Each RNA output  $R_i$  is designed to bind to the inhibitor  $I_j$  (domains indicated as  $q_j$ - $a_j$ - $t_j$ ), thereby releasing the activator  $A_j$  for binding to  $T_j$ . Because  $R_i$  should also cover the active domain of  $R_j$  in the formation of  $P$ , then  $R_i$  must also be complementary to  $A_i$  (domains  $t'_i$ - $a'_i$ - $q'_i$ ): therefore, this design is structurally affected by binding of RNA to templates (as for the self-repressing circuit), and by RNA-mediated self-inhibition loops, as shown in the reaction scheme in Figure S18 C. The entity of these design pitfalls depends on the length and sequences of the complementarity domains shared by  $R_i$  and  $R_j$ . For instance, we could avoid inserting in the RNA species the toehold sequences  $t_1$ ,  $t'_1$ ,  $t_2$ , and  $t'_2$  to minimize the self inhibition; however, this would facilitate the formation of complexes  $A_i \cdot I_i \cdot R_j$  that would slow down the release of  $A_i$ .

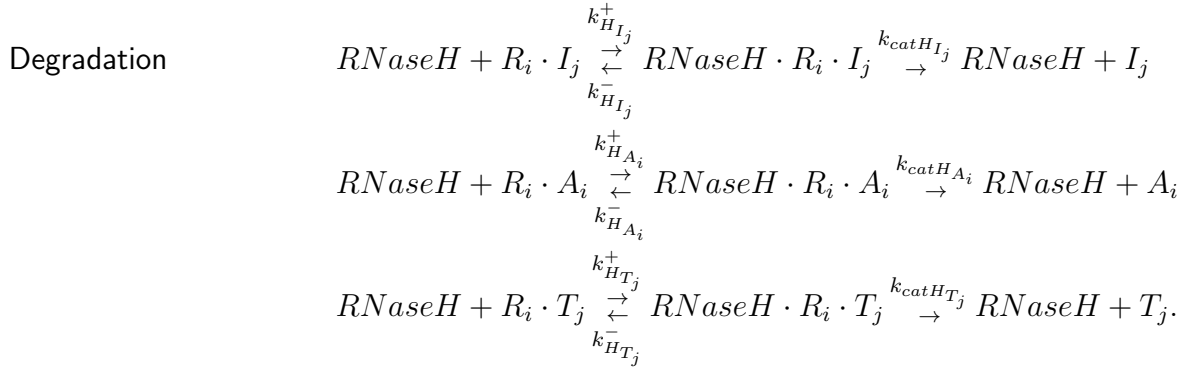
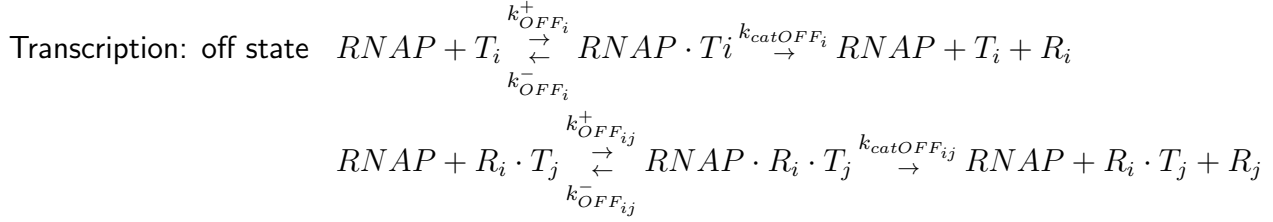
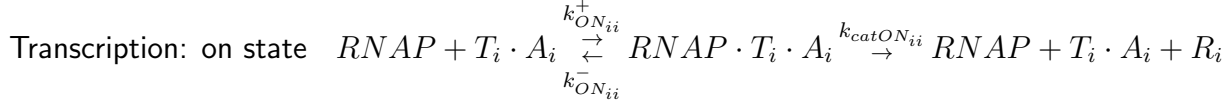
Preliminary experiments on this design, reported in Franco [2012], show that the issues described above are significant. In particular, the design could be improved if the self-inhibition pathways were minimized: this was attempted, without conclusive success, by increasing the concentration of DNA inhibitors, the concentration of RNase H, and by lengthening the length of toeholds for  $A_i$  and  $I_i$ . Experiments also highlighted the possibility of “leaky” transcription of inhibited switches. We refer the reader to Franco [2012], Chapter 1, for further details. Here, we only describe our numerical analysis, which suggests that the scheme has the ability to match transcription rates of two cross-activating genelets when we choose plausible reaction parameters.

#### 4.2.1 Modeling

To construct a dynamic model for the cross-activating circuit represented in Figure S18 A, we start from a list of all the chemical reactions that can occur,

Activation	$T_i + A_i \xrightarrow{k_{T_i A_i}} T_i \cdot A_i$
Inhibition	$T_i \cdot A_i + I_i \xrightarrow{k_{T_i A_i I_i}} T_i + I_i \cdot A_i$
Annihilation	$A_i + I_i \xrightarrow{k_{A_i I_i}} A_i \cdot I_i$
Release	$R_i + A_j \cdot I_j \xrightarrow{k_{R_i A_j I_j}} R_i \cdot I_j + A_i$
Annihilation	$R_i + I_j \xrightarrow{k_{R_i I_j}} R_i \cdot I_j$
Output formation	$R_i + R_j \xrightarrow{k_{R_i R_j}} R_i \cdot R_j$
Undesired interactions	$R_i + A_i \xrightarrow{k_{R_i A_i}} R_i \cdot A_i$
	$R_i + T_j \xrightarrow{k_{R_i T_j}} R_i \cdot T_j$





The resulting set of ordinary differential equations is:

$$\begin{aligned}
 \frac{d}{dt}[T_i] &= -k_{T_i A_i}[T_i][A_i] - k_{R_j T_i}[R_j][T_i] + k_{T_i A_i I_i}[T_i \cdot A_i][I_i] + k_{catHT_i}[RNaseH \cdot R_j \cdot T_i], \\
 \frac{d}{dt}[A_i] &= -k_{T_i A_i}[T_i][A_i] - k_{A_i I_i}[A_i][I_i] - k_{R_i A_i}[R_i][A_i] + k_{catHA_i}[RNaseH \cdot R_i \cdot A_i], \\
 \frac{d}{dt}[I_i] &= -k_{A_i I_i}[A_i][I_i] - k_{T_i A_i I_i}[T_i \cdot A_i][I_i] - k_{R_j I_i}[R_j][I_i] + k_{catHI_i}[RNaseH \cdot R_j \cdot I_i], \\
 \frac{d}{dt}[R_i] &= -k_{R_i A_j I_j}[R_i][A_j \cdot I_j] - k_{R_i R_j}[R_i][R_j] - k_{R_i T_j}[R_i][T_j] - k_{R_i I_j}[R_i][I_j] - k_{R_i A_i}[R_i][A_i] \\
 &\quad + k_{catON_{ii}}[RNAP \cdot T_i \cdot A_i] + k_{catOFF_i}[RNAP \cdot T_i] + k_{catOFF_{ji}}[RNAP \cdot R_j \cdot T_i], \\
 \frac{d}{dt}[R_i \cdot T_j] &= +k_{R_i T_j}[R_i][T_j] - k_{catHT_j}[RNaseH \cdot R_i \cdot T_j], \\
 \frac{d}{dt}[R_i \cdot R_j] &= +k_{R_i R_j}[R_i][R_j].
 \end{aligned} \tag{11}$$

As previously done for the self-inhibiting circuit model, we can express the enzyme-substrate complexes using the Michaelis-Menten approximation. For the RNAP substrate, for instance, we find:

$$[RNAP \cdot T_i \cdot A_i] = \frac{[RNAP^{tot}]}{\left(1 + \sum_{i,j} \frac{[T_i \cdot A_i]}{k_{MON_{ii}}} + \frac{[T_i]}{k_{MOFF_i}} + \frac{[R_i \cdot T_j]}{k_{MOFF_{ij}}}\right)}. \tag{12}$$

Analogous expressions can be derived for all other complexes.

Equations (11) are numerically solved using the MATLAB ode23s solver. Table S4 shows the parameters used for the simulations. Such generic parameters are consistent with those in Kim



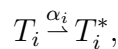
et al. [2006]. For simplicity we assume that the two sub-circuits are symmetric and have the same binding rates. We check the behavior of the system by creating an imbalance in the total concentration of inhibitors:  $[T_1^{tot}] = [A_1^{tot}] = 50$  nM,  $[T_2^{tot}] = [A_2^{tot}] = 100$  nM, while  $[I_1^{tot}] = 20$  nM and  $[I_2^{tot}] = 120$  nM. The simulation first allows for equilibration of all the DNA strands in the absence of enzymes. The plot shows the trajectories after addition of the enzymes, whose total concentration is assumed to be  $[RNAP^{tot}] = 80$  nM and  $[RNaseH^{tot}] = 8.8$  nM, based on typical experimental conditions. As noted before for the self-inhibitory scheme, the concentration of RNAP is not negligible relative to the total amount of genelets present and therefore the Michaelis-Menten approximation may not be accurate in this case. The simulation results are shown in Figure S19 and are consistent with the traces obtained for the simple model system shown at Figure S16 A: the templates cross-activate and reach an equilibrium where the flow of total RNA is matched. A comparison between the performance of the transcriptional negative and positive feedback circuits models was also done in Franco and Murray [2008].

Table S4: Parameters for the Initial Numerical Analysis of the Cross Activating Circuit

Units: $[1/M/s]$	Units: $[1/s]$	Units: $[M]$
$k_{T_i A_i} = 4 \cdot 10^4$	$k_{catON_{ii}} = 0.06$	$k_{MON_{ii}} = 250 \cdot 10^{-9}$
$k_{T_i A_i I_i} = 5 \cdot 10^4$	$k_{catOFF_i} = 1 \cdot 10^{-3}$	$k_{MOFF_i} = 1 \cdot 10^{-6}$
$k_{A_i I_i} = 5 \cdot 10^4$	$k_{catOFF_{ij}} = 1 \cdot 10^{-3}$	$k_{MOFF_{ij}} = 1 \cdot 10^{-6}$
$k_{R_j A_i I_i} = 5 \cdot 10^5$	$k_{catHI_i} = 0.1$	$k_{MHI_i} = 50 \cdot 10^{-9}$
$k_{R_i I_i} = 5 \cdot 10^5$	$k_{catHT_i} = 0.1$	$k_{MHT_i} = 50 \cdot 10^{-9}$
$k_{R_i T_j} = 1 \cdot 10^3$	$k_{catHA_i} = 0.1$	$k_{MHA_i} = 50 \cdot 10^{-9}$
$k_{R_i A_i} = 1 \cdot 10^3$		
$k_{R_i R_j} = 2 \cdot 10^5$		

## 5 Numerical scalability analysis of our simplified positive feedback scheme model for flux regulation

Here we report the mathematical models for positive feedback topologies in the case of  $n$  generating species  $T_i$ . This numerical study was initially outlined in Giordano et al. [2013]. The ODE systems were derived using mass action kinetics and used for the numerical simulation of the proposed topologies in the case of three-component networks. Positive feedback is implemented, as for smaller networks, with a cross-activation scheme: when an output is in excess (not used in the product formation), it increases the generation rate of all the other outputs it forms a product with:



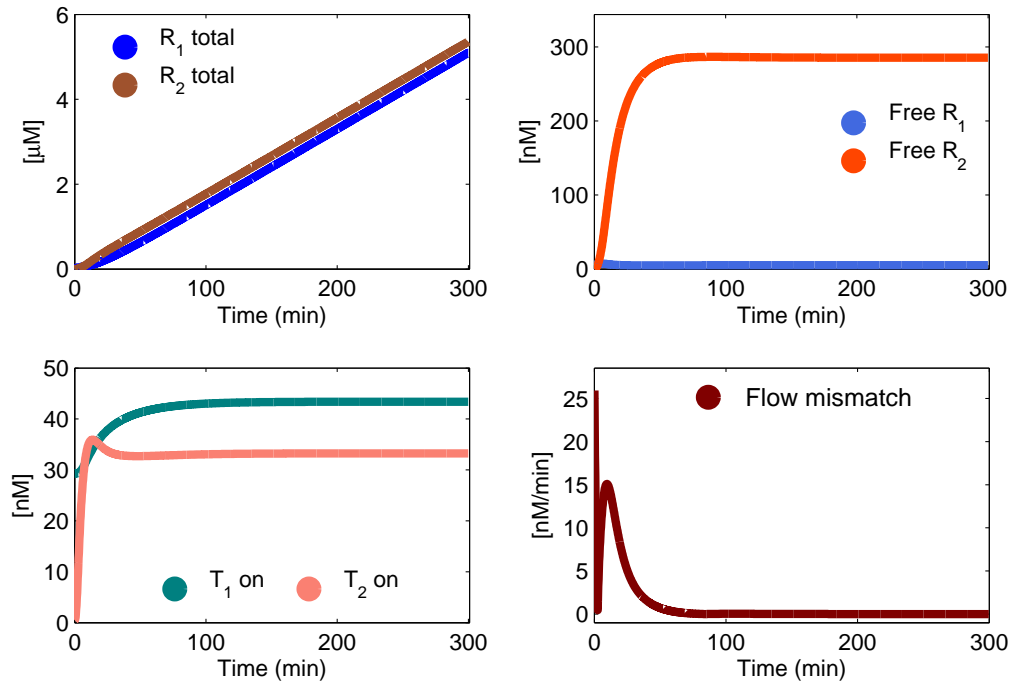


Figure S19: Numerical simulation for equations (11). Parameters are chosen as in Table S4.  $[T_1^{tot}] = [A_1^{tot}] = 50$  nM,  $[T_2^{tot}] = [A_2^{tot}] = 100$  nM, while  $[I_1^{tot}] = 20$  nM, and  $[I_2^{tot}] = 120$  nM.  $[RNAP^{tot}] = 80$  nM and  $[RNaseH^{tot}] = 8.8$  nM. These numerical results are in general consistent with those obtained for the simple model (6), shown in Figure S16 A.

where  $T_i^*$  is an inactive complex. We assume that  $[T_i^{tot}] = [T_i] + [T_i^*]$  and that the active complex  $T_i$  naturally inactivates with a first order rate  $\alpha_i$ .

## 5.1 Single product topology

In a single product topology, a single complex  $P$  is concurrently formed by all the  $n$  outputs:

$$\sum_{i=1}^n R_i \xrightarrow{k} P.$$

The corresponding differential equations are

$$\begin{aligned} \frac{d[T_i]}{dt} &= -\alpha_i [T_i] + \delta_i ([T_i^{tot}] - [T_i]) \prod_{j \neq i} [R_j] \\ \frac{d[R_i]}{dt} &= \beta_i [T_i] - k \prod_{i=1}^n [R_i] - \delta_i [R_i] \prod_{j \neq i} ([T_j^{tot}] - [T_j]) \\ \frac{d[P]}{dt} &= k \prod_{i=1}^n [R_i] \end{aligned} \quad (13)$$

and the total amount of  $R_i$  is  $[R_i^{tot}] = [R_i] + \sum_{j \neq i} [T_j] + [P]$ . The simulation results, in Figure S20 (a), show that also this feedback strategy is effective. The concentrations of active  $T_i$

asymptotically decrease and flow mismatches reduce, yet the time response is slower than in the negative feedback case. With respect to negative feedback, there is also a higher  $R_i$  production.

## 5.2 Handshake and neighbor topologies

Subcomponents generation is expressed by the reaction  $R_i + R_j \xrightarrow{k_{ij}} P_{ij}$  and positive feedback acts on gene  $i$  due to gene  $j$ :  $R_i + T_j^* \xrightarrow{\delta_{ij}} T_j$ . The differential equations are

$$\begin{aligned}\frac{d[T_i]}{dt} &= -\alpha_i [T_i] + \sum_j \delta_{ij} [R_j] ([T_i^{tot}] - [T_i]) \\ \frac{d[R_i]}{dt} &= \beta_i [T_i] - \sum_j k_{ij} [R_i][R_j] - \sum_j \delta_{ji} [R_i] ([T_j^{tot}] - [T_j]) \\ \frac{d[P_{ij}]}{dt} &= k_{ij} [R_i][R_j]\end{aligned}\tag{14}$$

and the total amount of  $R_i$  is  $[R_i^{tot}] = [R_i] + \sum_j [T_j] + \sum_j [P_{ij}]$ . We remind that the two topologies coincide in the case  $n = 3$ . The simulation results are shown in Figure S20 (b). The concentration of active genes decreases and the flux mismatches are reduced, but the response time is still longer than in the negative feedback architecture. Moreover, there is a higher  $R_i$  production than in the negative feedback case. We can note that the handshake/neighbor connection generates less waste (unused  $R_i$ ) than the single product interconnection.

## 5.3 Parameters

For the numerical solution, the parameters chosen are:  $k_{ij} = 2 \cdot 10^3$  /M/s for the handshake/neighbor topology and  $k = 6 \cdot 10^3$  /M/s for the single product topology,  $\delta_{ij} = 50$  /M/s,  $\alpha_i = 3 \cdot 10^{-4}$  /s,  $\beta_i = 1 \cdot 10^{-2}$  /s,  $[T_1^{tot}] = 100$  nM,  $[T_2^{tot}] = 200$  nM,  $[T_3^{tot}] = 300$  nM. An imbalance in the production rates of  $R_i$  is created by setting  $[T_i](0) = [T_i^{tot}]$ , while  $[R_i](0) = 0$ .

## 5.4 Performance overview of the different topologies as a function of key parameters

Using Figures S22 and S23 as a support, we can compare the performance of the positive feedback strategy for networks with  $n = 3$ . These topologies are shown in Figure S21; for  $n = 3$  the handshake and neighbor topology coincide, Figure S21 B.

We numerically analyzed the network response in terms of active percentage of  $T_i$ , mean flow mismatch and response time, defined as previously done for negative feedback topologies. We solved the differential equations for a time span of 10 hours and averaged the trajectories for active  $T_i$  and for the computed mismatch over the last simulation hour. We examined the sensitivity to variations in  $\delta$ , the feedback strength, and in  $\alpha$ , the rate of spontaneous inactivation of  $T_i$ :  $\delta$  varies from a hundredth to a hundred times its nominal value;  $\alpha$  varies from a hundredth of its nominal value to twice its nominal value, and up to five times its nominal value in the response time analysis. In each figure, a pink square highlights the system behavior when the nominal parameters in Section 5.3 are adopted.

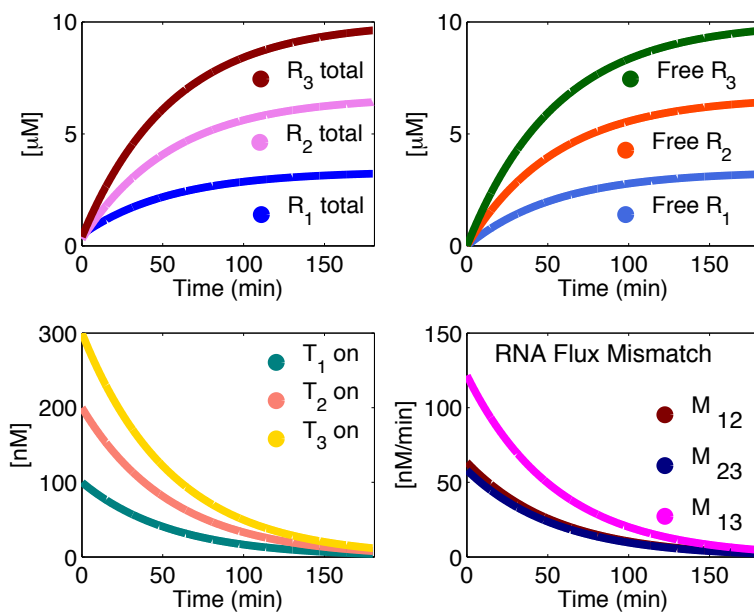
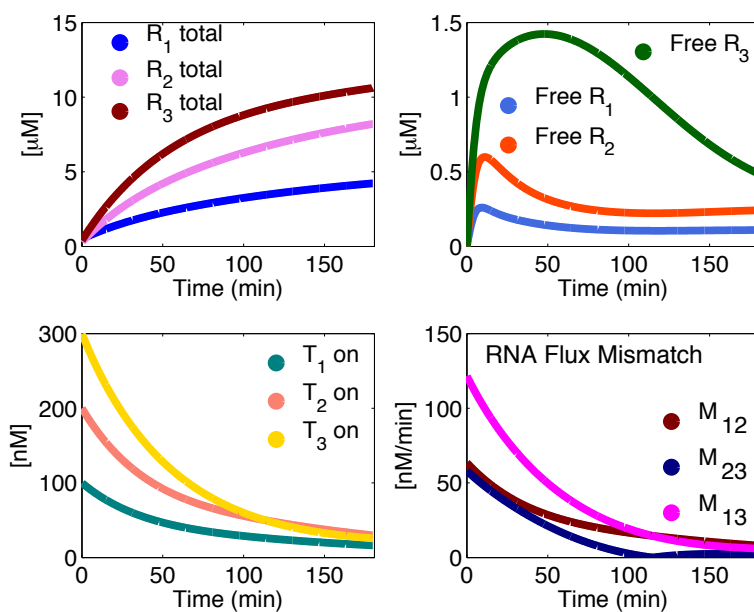
(a) single product topology,  $n = 3$ (b) handshake/neighbor topologies,  $n = 3$ 

Figure S20: Example traces from numerical simulations: positive feedback scheme.



Figure S21: A: Single product topology. B: Handshake/neighbor interconnection.

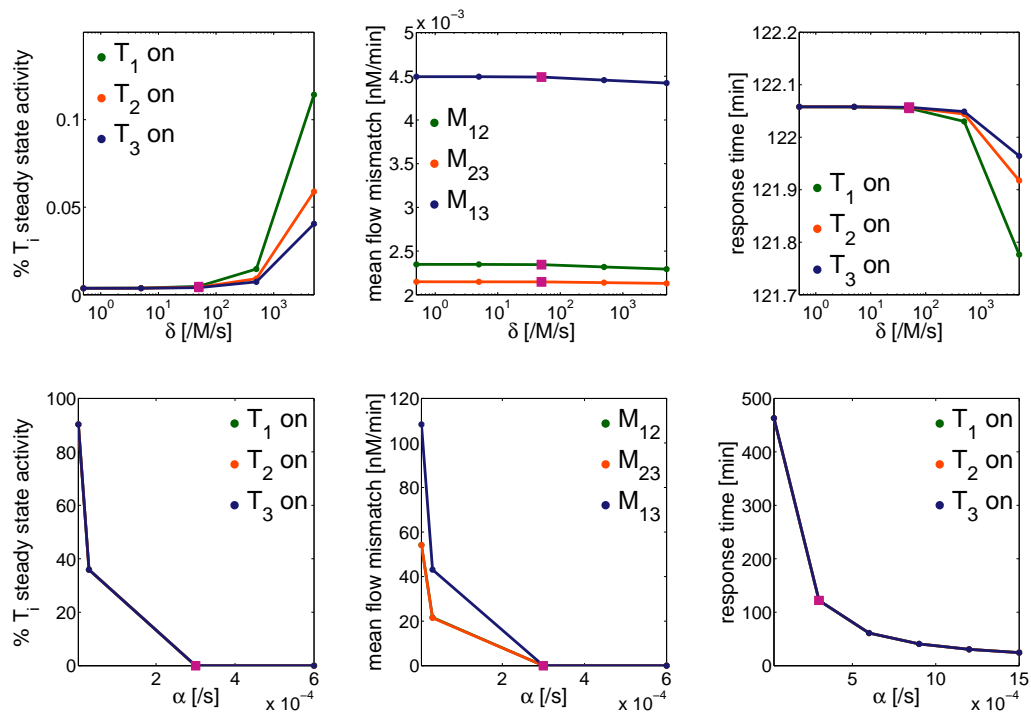


Figure S22: Positive feedback, single product topology: parameter sensitivity analysis.

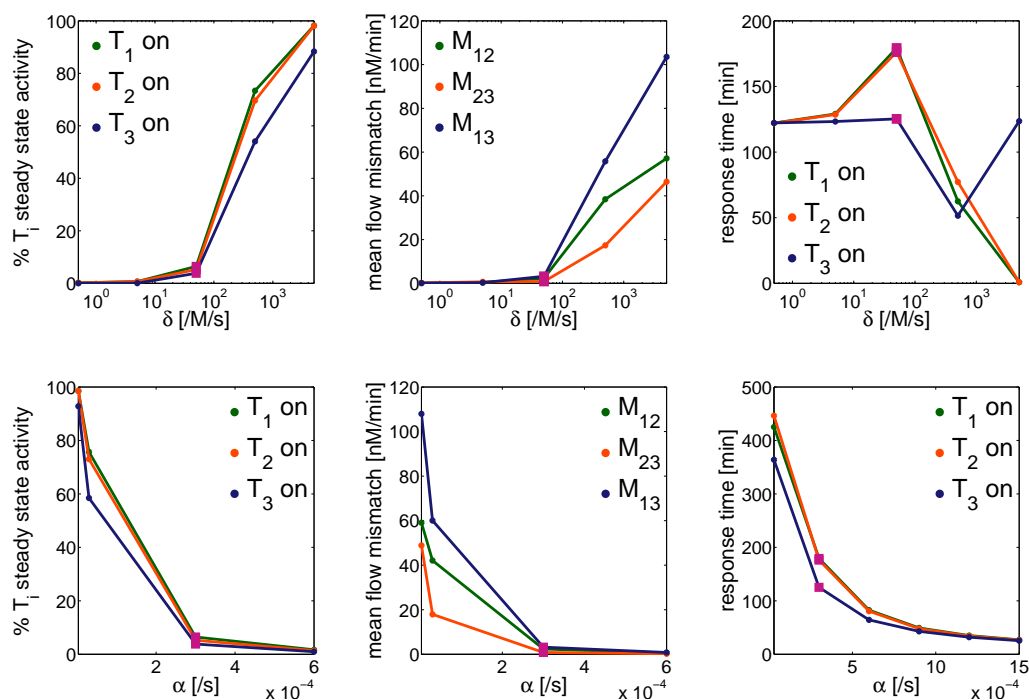


Figure S23: Positive feedback, neighbor/handshake topology: parameter sensitivity analysis.

In all network topologies, an increase in the spontaneous inactivation parameter  $\alpha$  yields a lower mismatch, decreases the response time and considerably reduces the steady state activity of  $T_i$ . In the handshake/neighbor topology, an increase in the positive feedback parameter  $\delta$  yields a significantly higher  $T_i$  steady state activity and a larger mismatch; in the single product topology, instead, the steady state activity of  $T_i$  is quite low and almost insensitive to variations in  $\delta$  and the mismatch is almost independent of  $\delta$ . When  $\delta$  increases, the response time decreases in the single product topology, while it does not have a monotone behavior in the handshake/neighbor topology.

## References

Integrated DNA technologies: <http://www.idtdna.com>. URL <http://www.idtdna.com>.

- E. Franco. *Analysis, design, and in vitro implementation of robust biochemical networks*. PhD thesis, California Institute of Technology, 2012.
- E. Franco and R. M. Murray. Design and performance of *in vitro* transcription rate regulatory circuits. In *Proceedings of the IEEE Conference on Decision and Control*, 2008.
- E. Franco, P.-O. Forsberg, and R. M. Murray. Design, modeling and synthesis of an *in vitro* transcription rate regulatory circuit. In *Proceedings of the American Control Conference*, 2008.
- E. Franco, E. Friedrichs, J. Kim, R. Jungmann, R. Murray, E. Winfree, and F. C. Simmel. Timing molecular motion and production with a synthetic transcriptional clock. *Proceedings of the National Academy of Sciences*, 108(40):E784–E793, 2011.
- G. Giordano, E. Franco, and R. M. Murray. Feedback architectures to regulate flux of components in artificial gene networks. In *Proceedings of the American Control Conference*, 2013.
- J. Kim. *In vitro synthetic transcriptional networks*. PhD thesis, California Institute of Technology, 2007.
- J. Kim and E. Winfree. Synthetic *in vitro* transcriptional oscillators. *Molecular Systems Biology*, 7:465, 2011.
- J. Kim, K. S. White, and E. Winfree. Construction of an *in vitro* bistable circuit from synthetic transcriptional switches. *Molecular Systems Biology*, 1:68, 2006.
- S. Milburn, M. Goldrick, and M. Winkler. Compositions and methods for increasing the yields of *in vitro* RNA transcription and other polynucleotide synthetic reactions, U. S. Patent 5256555, 1993.
- J. N. Zadeh, C. D. Steenberg, J. S. Bois, B. R. Wolfe, M. B. Pierce, A. R. Khan, R. M. Dirks, and N. A. Pierce. NUPACK: analysis of nucleic acid systems. *Journal of Computational Chemistry*, 32:170–173, 2011.
- M. Zuker and P. Stiegler. Optimal computer folding of large RNA sequences using thermodynamics and auxiliary information. *Nucleic Acids Research*, 9(1):133–148, 1981.